Author Manuscript
Author Manuscript
Author Manuscript
Author Manuscript

HHS Public Access
Author manuscript
Nat Microbiol. Author manuscript; available in PMC 2023 March 10.

Published in final edited form as:
Nat Microbiol. 2023 February ; 8(2): 284–298. doi:10.1038/s41564-022-01315-5.

Structure of *Geobacter* cytochrome OmcZ identifies mechanism of nanowire assembly and conductivity

Yangqi Gu[1,2,8], **Matthew J. Guberman-Pfeffer**[1,3], **Vishok Srikanth**[1,3], **Cong Shen**[1,4], **Fabian Giska**[5,6], **Kallol Gupta**[5,6], **Yuri Londer**[1,3], **Fadel A. Samatey**[1,3], **Victor S. Batista**[7], **Nikhil S. Malvankar**[1,3]

[1]Microbial Sciences Institute, Yale University, West Haven, CT, USA.

[2]Department of Molecular, Cellular and Developmental Biology, Yale University, New Haven, CT, USA.

[3]Department of Molecular Biophysics and Biochemistry, Yale University, New Haven, CT, USA.

[4]Department of Microbiology, Yale University, New Haven, CT, USA.

[5]Department of Cell Biology, Yale University, New Haven, CT, USA.

[6]Nanobiology Institute, Yale University, West Haven, CT, USA.

[7]Department of Chemistry, Yale University, New Haven, CT, USA.

[8]Present address: PNAC division, Medical Research Council Laboratory of Molecular Biology, Cambridge, UK.

Abstract

OmcZ nanowires produced by *Geobacter* species have high electron conductivity (>30 S cm^{-1}). Of 111 cytochromes present in *G. sulfurreducens,* OmcZ is the only known nanowire-forming cytochrome essential for the formation of high-current-density biofilms that require long-distance (>10 μm) extracellular electron transport. However, the mechanisms underlying OmcZ nanowire assembly and high conductivity are unknown. Here we report a 3.5-Å-resolution

Reprints and permissions information is available at www.nature.com/reprints.

Correspondence and requests for materials should be addressed to Yangqi Gu or Nikhil S. Malvankar. ygu@mrc-lmb.cam.ac.uk; nikhil.malvankar@yale.edu.

Author contributions
Y.G. purified OzpA, $OmcZ_{50}$ and OmcZ nanowires, collected and analysed negative-stain and cryo-EM data to build the atomic model, performed biochemical analyses, UV–vis, CD spectroscopy, solubility test, nanowire alignment, in vitro digestion experiment of OmcZ nanowires, immune-gold labelling and power spectra analyses. M.J.G.-P. performed molecular dynamics and CD simulations. Y.L. constructed the expression vector for $OmcZ_{50}$ in *E. coli.* Y.G. and F.A.S. optimized the culturing condition and purified $OmcZ_{50}$ from *E. coli.* V.S. helped with OmcZ nanowire purification. F.A.S. and V.S. helped with model building. C.S. constructed the *omcS:pk18* strain for OmcZ purification. F.G. performed the native mass spectrometry experiments and analysed the data under the supervision of K.G. V.S.B. guided computational studies. Y.G. and N.S.M. conceived and designed the project. N.S.M. supervised the work. Y.G. and N.S.M. wrote the paper with input from all the authors.

Competing interests
The authors declare no competing interests.

Extended data is available for this paper at https://doi.org/10.1038/s41564-022-01315-5.

Supplementary information The online version contains supplementary material available at https://doi.org/10.1038/s41564-022-01315-5.

Reporting summary
Further information on research design is available in the Nature Portfolio Reporting Summary linked to this article.

Author Manuscript Author Manuscript Author Manuscript Author Manuscript

cryogenic electron microscopy structure for OmcZ nanowires. Our structure reveals linear and closely stacked haems that may account for conductivity. Surface-exposed haems and charge interactions explain how OmcZ nanowires bind to diverse extracellular electron acceptors and how organization of nanowire network re-arranges in different biochemical environments. In vitro studies explain how *G. sulfurreducens* employ a serine protease to control the assembly of OmcZ monomers into nanowires. We find that both OmcZ and serine protease are widespread in environmentally important bacteria and archaea, thus establishing a prevalence of nanowire biogenesis across diverse species and environments.

Long-range (>10 μm) extracellular transport of respiratory electrons along networks of protein filaments, called microbial nanowires, has applications for bioremediation, bioenergy and bioelectronics[1] and drives a wide range of globally important environmental phenomena that influence carbon and mineral cycling in soils and sediments, bioremediation, corrosion and anaerobic conversion of organic wastes to methane or electricity[2,3]. The common soil bacterium *Geobacter* has proven to be a useful model for studying long-range microbial electron transport because it directly contacts extracellular electron acceptors[4] or syntrophic partner species[3] using protein nanowires[5-7]. Structural, functional and cellular localization studies have shown that nanowires present on the surface of electricity-producing wild-type (WT) *Geobacter sulfurreducens* comprise cytochromes OmcS[8,9] and OmcZ[10,11], whereas strains with genetically modified OmcS grown under conditions that do not require extracellular electron transport produce filaments of cytochrome OmcE[12]. Furthermore, *G. sulfurreducens* pili are required for the secretion of OmcS and OmcZ nanowires[1,13].

Out of 111 predicted *c*-type cytochromes present in the 3.8 Mb genome of *G. sulfurreducens,* OmcZ is the only nanowire-forming outer-surface cytochrome that has been experimentally proven to enable long-range (>10 μm) electron transport[14], highlighting its importance over other OmcS nanowire-like cytochromes that are abundant in soil[15].

Using a combination of immunogold labelling with a suite of biochemical and biophysical experiments, we previously reported that *G. sulfurreducens* can assemble highly conductive OmcZ nanowires, and that external application of electric fields to biofilms grown on electrodes stimulates bacterial production of OmcZ nanowires[10]. The extremely high conductivity (>30 S cm^{-1}) of OmcZ nanowires and their concentration[16] adjacent to the biofilm–electrode interface is correlated with maximum observed metabolic activity of *G. sulfurreducens* cells[17]. Prior genetic, electrochemical and spectroscopic studies have suggested a crucial role for OmcZ in extracellular respiration[11,18,19] by a mechanism that differs from diffusing shuttle molecules that are produced by other bacteria[20]. Shuttles limit the electrocatalytic performance of other bacteria[20,21]. Synthetically embedding silver nanoparticles in the outer cell membrane improves electric power for shuttle-producing species[21], whereas similar power is generated by WT *G. sulfurreducens* via nanowires[22]. Thus, in addition to physiological role in long-range respiration and ecological role in enabling bacteria to form biofilm communities, OmcZ nanowires enable bacteria to produce the highest electric power by pure culture[23,24] and form >100-μm-thick conductive biofilm communities[14,25,26]. However, the mechanism underlying the ability of OmcZ

Author Manuscript Author Manuscript Author Manuscript Author Manuscript

nanowire networks in biofilms to transport electrons over 100 times bacterial length is not known. Understanding the molecular mechanisms of OmcZ nanowire's assembly and high conductivity will inspire novel strategies to improve bacterial extracellular respiration using these living electronic materials.

In this Article, we use a combination of structural and functional studies using a suite of genetic, biochemical, biophysical and computational methods to identify the mechanism of how OmcZ nanowires assemble and conduct electricity.

Results

OmcZ structure reveals linear and closely stacked haems

All prior studies on OmcZ nanowires also contained nanowires of other cytochromes[27,28], making it difficult to achieve high-resolution structure or perform any bulk functional studies. To obtain pure OmcZ nanowires without any contamination from other nanowires, we disrupted *omcS* in *G. sulfurreducens* CL-1 that forms highly conductive biofilms[29] (Supplementary Table 1, Methods). We sheared nanowires from pelleted cells using blending to purify them away from pili filaments which are present in the supernatant[13]. Next we purified OmcZ n anowires using a sucrose gradient and size exclusion chromatography (Fig. 1a). We used sodium dodecyl sulfate–polyacrylamide gel electrophoresis (SDS–PAGE) gel with Coomassie staining and negative-stain transmission electron microscopy (TEM) to validate the purity of nanowires (Fig. 1b,c) and proceeded to analyse pure OmcZ nanowires using cryogenic electron microscopy (cryo-EM) (Fig. 1d,e)

We obtained a 3.5-Å-resolution cryo-EM structure for purified OmcZ nanowires using iterative helical real space reconstruction (Fig. 1f,g, Extended Data Fig. 1 and Extended Data Table 1a). The structure has a left-handed one-start helix, with a helical rise of 57.4 Å and a rotation of −159.1°. At this resolution, the backbone density along with many bulky sidechain densities, such as aromatic residues and all eight haem densities, are visible (Fig. 1h and Extended Data Fig. 1a-j). Cells produce two forms of OmcZ: the 50 kDa precursor ($OmcZ_{50}$) and nanowire-forming 30 kDa ($OmcZ_{30}$). The cryo-EM model enabled us to trace the C_α backbone for each protomer subunit and thread $OmcZ_{30}$ sequence with all 258 amino acids and 8 haems[30]. OmcZ contains ~12% helices and ~28% β-strands and turns (~21% strands and ~7% turns), which is higher than ~22% β-strands and turns found in OmcS (~5.7% β strands, 16.7% turns), consistent with prior secondary structure studies[10].

OmcZ subunits have a compact and linear structure with a smaller diameter (~23 Å) than OmcS nanowires[8] (~35 Å) (Fig. 1f). Owing to its compactness, the haems in the OmcZ nanowire are closely stacked with edge-to-edge distances substantially smaller than haems in OmcS nanowires, consistent with data by grazing-incidence X-ray diffraction that detects π-stacking in soft materials[10]. Parallel-stacked haems are ~0.3 Å closer and perpendicularly (T)-stacked haems are ~1 Å closer in OmcZ compared with in OmcS (Fig. 2a,b and Extended Data Table 1b).

Closer stacking of haems in OmcZ may be due to conserved amino acid residues adjacent to haems (Fig. 2c,d). In particular, three pairs of histidines are evolutionarily conserved across

Author Manuscript Author Manuscript Author Manuscript Author Manuscript

all OmcZ homologues analysed (Fig. 2e,f and Extended Data Fig. 2). Structure revealed that these histidine pairs lock T-stacked haems more tightly together than those found in OmcS (Fig. 2a,b and Extended Data Table 1b). We hypothesize that high electronic conductivity of OmcZ may be partly due to closer distance between T-stacked haems, which typically have ~10 times lower electronic coupling (ceteris paribus, 100 times lower electron transfer rate) than parallel-stacked haems[31]. c3 cytochromes from *Desulfovibrio* species also have similar haem structures (Protein Data Bank (PDB) IDs: 1gyo, 2bq4 and 2e84) (ref. [10]). The amino acid sequence of c3 contains CXXCHH motif with one proximal and one distal histidine in the haem pairs while OmcZ contains two distal histidines. All four structures have consecutive histidines causing tight haem T-junction with similar haem–haem distances[10]. However, none of the c3 cytochromes is known to form nanowires.

To compare the haem–haem interactions in OmcZ and OmcS nanowires, we used circular dichroism (CD) spectroscopy. CD spectra of OmcZ nanowires at pH 7 were similar to pH 10.5 used to solve the atomic structure (Extended Data Fig. 3a), indicating similar OmcZ structures at these pH values. CD measurements of OmcZ nanowires and computational predictions of haem interactions in OmcZ using density functional theory (DFT) identified a peak instead of valley at 406 nm, which indicates that haem–haem interactions in OmcZ are different than in OmcS (Extended Data Fig. 3b-i). These analyses confirm that the haem arrangement in OmcZ enables specific haem–haem interactions.

Haem loop traps diverse extracellular electron acceptors

In OmcZ, haems I–V and VII form a linear, central, electron transport chain whereas haem VI is surface exposed (Figs. 2a and 3a). In addition, haems in OmcZ have more solvent exposure than haems in OmcS (Fig. 3a,b). For example, the structure reveals fully exposed haem VI and partially exposed haems I and II that can make more contact with electron acceptors and electrodes for low contact resistance and higher conductivity of OmcZ nanowires than OmcS nanowires. Therefore, both the closer stacking of haems and their higher surface exposure in OmcZ may account for the higher conductivity measured for individual OmcZ[10] than OmcS[31] nanowires using conducting-probe atomic force microscopy as well as high conductivity measured for individual nanowires produced by strain W51W57 (ref. [32]) (shown to be OmcZ nanowires[10]).

Furthermore, all haems in OmcZ are anchored to the protein backbone by haem-binding motifs (CXXCH) except for haem II, which is attached by a non-canonical haem-binding motif that has 12 additional residues ($CX_{14}CH$) between cystines 53 and 68 in OmcZ but not in OmcS (Fig. 3c,d). These 12 residues in OmcZ form a solvent-exposed loop, which might trap small molecules as electron acceptors and transfer electrons from haem II. Using reconstituted OmcZ, we find that deletion of the haem II loop reduces the rate of electron transfer by OmcZ nanowires to extracellular electron acceptors compared with the WT (Fig. 3e,f). Therefore, our structure explains the ability of OmcZ to reduce diverse physiologically important electron acceptors[30] with high conductivity. Higher solvent exposure in OmcZ compared with OmcS is also consistent with more negative reduction potential of OmcZ[30] compared with OmcS[33].

Author Manuscript Author Manuscript Author Manuscript Author Manuscript

OmcZ with severely modified sequence[34] can reduce riboflavin in vitro. Sequence modification could have also prevented nanowire formation. We found that purified OmcZ nanowires do not reduce riboflavin (Extended Data Fig. 4b). Our finding is consistent with the prior studies that redox cycling of flavins is primarily associated with the cytochromes in the outer membrane rather than nanowires[35].

Despite higher conductivity and solvent exposure of haems, OmcZ is not essential for bacterial reduction of Fe(III) oxide, an extracellular electron acceptor abundant in soil[36]. Furthermore, in prior studies, OmcZ monomers could not reduce Fe(III) oxide[30], which could be due to harsh conditions used in purification altering the OmcZ structure. To understand the binding of OmcZ and OmcS nanowires to Fe(III) oxide, we compared the surface charge of OmcZ and OmcS with Fe(III) oxide. At physiological pH, the surface charge of OmcZ nanowires is mostly negative, whereas OmcS nanowires have a positively charged pocket (Fig. 3g), in comparison with negatively charged Fe(III) oxide[37]. Furthermore, OmcZ was not fully reduced by dithiothreitol (DTT) (Extended Data Fig. 4b), suggesting that OmcZ contains low-reduction-potential haems that could affect the thermodynamics and kinetics of electron transfer. These differences in surface charge and redox potentials could explain slower reduction of Fe(III) oxide by OmcZ nanowires than OmcS nanowires (Fig. 3h).

Environment re-arranges organization of nanowire network

Despite their negative surface charge, cell-attached OmcZ nanowires form a network under physiological conditions (Fig. 4b), such as in electrode-grown biofilms[10], possibly due to the stacking of surface-exposed haems. This ability of OmcZ nanowires to form network has important implications in bacterial physiology. For example, our studies show that such a network can trap and reduce diverse extracellular electron acceptors[30,36] such as Fe(III) citrate and Fe(III) oxide (Fig. 3e,f,h and Extended Data Fig. 4). Furthermore, network of OmcZ nanowires in biofilms could explain their ability to conduct electrons over 100 times bacterial length[2].

We further found that the organization of OmcZ nanowire network re-arranges in different biochemical environments. The solubility of OmcZ nanowires decreases with increasing salt concentration (Fig. 4a,c,d). Nanowires remain soluble at low (<10 mM) salt concentrations and start aggregating into precipitating networks at high concentrations. Notably, the precipitation is fully reversible, which could help bacteria to reversibly switch the aggregation state of the network in response to the environmental changes. We built ordered arrays using the ability of OmcZ nanowires to aggregate into networks (Fig. 4c-e). For example, we assembled OmcZ nanowires into C-shaped arrays using a positively charged hexamethylenediamine-based self-assembly[38] (Fig. 4e).

Furthermore, we found that purified OmcZ nanowires remain stable when treated with various denaturants including urea, sodium dodecyl sulfate (SDS), and guanidine chloride (GuHCl), or incubated at acidic pH 1.6 (Extended Data Fig. 5). The stability of OmcZ nanowires is probably due to its negative surface charge (Fig.3a), which may prevent binding to denaturing agents (such as SDS) that are also negatively charged. The propensity of OmcZ nanowires to form networks (Fig. 4b) might also prevent other denaturing

Author Manuscript Author Manuscript Author Manuscript Author Manuscript

agents (such as GuHCl) from accessing the OmcZ surface. Furthermore, OmcZ nanowires show unique self-assembly mechanism by polymerization primarily using hydrophobic interactions and haem and aromatic stacking at the interface (Fig. 5a-d), whereas most denaturing agents, such as urea, GuHCl and low pH, destabilize protein by targeting hydrogen bonding. Therefore, stability of OmcZ nanowires could be due to negative surface charge, propensity to form networks and polymerization primarily via stacking interactions. We propose that purified OmcZ nanowires could form the basis of electronic biomaterials for use in acidic or protein-denaturing environments.

Assembly of OmcZ nanowire is proteolytically controlled

Our structural analyses showed that OmcZ nanowires have a protomer interface stabilized by four different interactions (Fig. 5a-d), but lack the inter-protomer metal coordination present in OmcS nanowires[8] or OmcE filaments[12]. To understand how OmcZ nanowires assemble, we characterized self-assembly of OmcZ nanowires in vitro. Previously, it was reported that *G. sulfurreducens* uses a serine protease, named OzpA (OmcZ protease), to cleave the precursor $OmcZ_{50}$ into nanowire-forming $OmcZ_{30}$ and that this cleavage is essential for extracellular electron transfer[39]. However, the cleavage process and its role in assembly of OmcZ into nanowires was not fully elucidated.

We found that purified OzpA cleaves both native and recombinant $OmcZ_{50}$ into $OmcZ_{30}$ which then self-assembled into nanowires (Fig. 5e-i and Extended Data Figs. 6 and 7). Notably, reconstituted OmcZ nanowires after proteolytic cleavage had structures that were indistinguishable from native nanowires on the basis of a power spectrum analysis (Fourier transform of the sample images) and 2D average (Fig. 5h,i and Extended Data Fig. 6e,f). Our in vitro studies therefore suggest that the protease serves as a molecular switch that regulates the assembly of OmcZ nanowires.

We next built a model of nanowire precursor $OmcZ_{50}$ using AlphaFold[40] (Fig. 5j and Supplementary Video 1). The predicted structure of the $OmcZ_{30}$ domain in $OmcZ_{50}$ was similar to the cryo-EM structure (Fig. 5l). We identified an extra domain in the predicted structure of $OmcZ_{50}$ (shaded in purple in Fig. 5j,k) that resembles a sugar-binding domain from other bacterial proteins such as dietary fibre used by *Bacteroidetes*[41]. This domain is expected to prevent polymerization of $OmcZ_{30}$ into nanowires by blocking a region where two protomers interact to form nanowires (Fig. 5a-d) but to increase the solubility of $OmcZ_{50}$. The presence of this extra domain might therefore explain the inability of $OmcZ_{50}$ to polymerize into nanowires. In addition to preventing polymerization, the sugar-binding domain may enable localization and secretion of $OmcZ_{50}$. This domain might localize $OmcZ_{50}$ in the periplasmic glycan layer, or in the outer membrane (where it might bind to OzpA to initiate OmcZ polymerization). Interestingly *G. sulfurreducens* pili have surface sugars and are required for OmcZ secretion[13]. We propose that this sugar-binding domain of $OmcZ_{50}$ may bind to pili during OmcZ nanowire secretion.

We next built a computational model of the OzpA-$OmcZ_{50}$ complex using AlphaFold[40] (Fig. 5m,n and Supplementary Video 1). Our model of OzpA placed the catalytic triad (His, Asp and Ser) of OzpA near Asn 258, in a position suitable for cleaving the extra domain from $OmcZ_{50}$ to form $OmcZ_{30}$. $OmcZ_{50}$ is found in the periplasmic and outer-membrane spaces

Author Manuscript Author Manuscript Author Manuscript Author Manuscript

of *G. sulfurreducens,* whereas $OmcZ_{30}$ is mainly found in the outer-membrane space rather than the periplasm[30]. OzpA is predicted to localize primarily in the outer-membrane and extracellular space[39]. We propose that OzpA cleaves $OmcZ_{50}$ in the outer membrane so that OmcZ nanowires can self-assemble on the cell surface (Fig. 4e-i).

omcZ homologues are widespread in bacteria and archaea

Cytochrome nanowires have been reported only in *G. sulfurreducens* and *omcZ* homologues were thought to be rare because not all *Geobacter* species show OmcZ homologues[42]. To evaluate whether there are *omcZ*-like genes in other microbes, we analysed the entire *omcZ* gene cluster, and our bioinformatic analysis revealed that diverse environmentally important bacteria and archaea have *omcZ*-like genes next to *ozpA* (Fig. 6 and Extended Data Fig. 9).

Using PCR with reverse transcription (RT–PCR) (Extended Data Fig. 8b), we confirmed co-transcription of *omcZ* and *ozpA* in *G. sulfurreducens* and found both genes in an operon of three genes encoding genes for nanowire precursor $OmcZ_{50}$, OzpA[39], which cleaves $OmcZ_{50}$ into nanowire-forming $OmcZ_{30}$ (Fig. 5e-i), and a peptidylprolyl *cis–trans* isomerase (GSU2074) required for the translation and processing of proline-rich proteins[43] (Fig. 5c). The amino acid sequence of $OmcZ_{30}$ contains 22 prolines[30]. Therefore, the prolyl isomerase is probably required for proper folding of $OmcZ_{30}$ into the correct conformation pre-polymerization which might explain why isomerase is essential for bacterial growth on electrodes[43]. All three genes in the *omcZ* operon are essential for the bacterial growth on electrodes. The 121 bp intergenic region between *omcZ* and *ozpA* is predicted to form extensive stem–loops on the messenger RNA and may suppress translation of *ozpA* by preventing the ribosome binding, unless triggered by an external stimulus[10], thus controlling the assembly of OmcZ nanowires (Extended Data Fig. 8a,c).

Our amino acid sequence alignment of *omcZ* homologues revealed complete conservation of all eight haem binding motifs (Extended Data Fig. 2)[44]. Notably, substantial sequence identity for several other residues was also observed throughout the sequence. For example, conserved residues include consecutive histidine pairs, which form a tight T-junction (Fig. 2e,f), and several prolines (in agreement with the conserved prolyl isomerase in the *omcZ* operon) (Fig. 6c).

Remarkably, using a combination of bioinformatics and AlphaFold, we found *omcZ* operon-like gene clusters, and OmcZ-like nanowire structures predicted in diverse methanogenic archaea that are the primary source of biogenic methane, such as *Methanosarcinales* (isolate METP1), as well as anaerobic methanotrophic (ANME) archaea, and nitrate-reducing freshwater ANME relatives (*Candidatus Methanoperedens nitroreducens*, ANME-2d), which consume methane released in marine sediments[44] that show high conductivity[45] (Fig. 6a,c and Extended Data Fig. 9). Furthermore, *omcZ* was one of the most highly transcribed genes in cultures grown under the conditions of anaerobic methane oxidation[44]. AlphaFold predictions of these *omcZ*-homologue nanowires showed haem arrangement similar to that in cryo-EM structure of OmcZ nanowire (Fig. 6c). As methane is the most abundant hydrocarbon[44], we propose that diverse microbes might use OmcZ-like nanowires for globally important processes, such as regulating atmospheric methane levels. High nanowire

Author Manuscript Author Manuscript Author Manuscript Author Manuscript

conductivity would explain the ability of these microbes to transfer electrons rapidly at rates too fast for molecular diffusion[46,47].

Our in vitro experiments showed that OzpA cleaves $OmcZ_{50}$ to release $OmcZ_{30}$, which self-assembles into nanowires that have similar structures to native OmcZ nanowires (Fig. 4e-i). Furthermore, along with OmcZ, the OzpA serine protease is essential for extracellular electron transfer to electrodes by *G. sulfurreducens*[39]. We found that the ozpA gene is conserved across all bacterial species that contain OmcZ homologues (Fig. 6c and Extended Data Fig. 2). Finally, amino acid sequences of predicted archaeal *omcZ* homologues show remarkably high (up to 68%) similarity to OmcZ, with conservation of all haem-binding motifs and residues involved in high conductivity (Extended Data Fig. 2). Therefore, it is likely that diverse bacteria and archaea use mechanisms similar to *G. sulfurreducens* to control the assembly of OmcZ nanowires.

Conclusions

Using a combination of structural, bioinformatic, computational and functional studies, we identify the mechanism of high conductivity and self-assembly of OmcZ nanowires to explain their physiological and ecological roles. Our studies also suggest a previously unknown strategy by which bacteria prevent aggregation of $OmcZ_{50}$ and assemble OmcZ nanowires on-demand. Our in vitro studies showed that the serine-protease OzpA cleaves $OmcZ_{50}$ to release $OmcZ_{30}$, which self-assembles into nanowires for long-distance electron transport in biofilms. Protein nanowires can serve as a template for other conductive materials[38,48]. As *G. sulfurreducens* biofilms also function as living transistors[2], supercapacitors[49] and photoconductors, due to ultrafast (~200 fs) electron transfer in cytochrome nanowires[50], we predict that robust performance of OmcZ nanowires may find novel bioelectronic applications.

Methods

Bacterial strain construction for purification of OmcZ nanowires

OmcZ nanowires were purified by constructing a *G. sulfurreducens omcS:pk18* strain using CL1 as a background strain[29]. *omcS:pk18* was constructed using a plasmid disruption protocol as previously described[51]. Briefly, we introduced an external plasmid pK18mobsacB to disrupt the *omcS* gene so that the strain will still produce OmcZ nanowires but not express OmcS. By the forward primer (5′-GTGACACCGGTCCTTCCAGCTA-3′) and the reverse primer (5′-CAGTTCACGTTGCTGGTGGC-3′), 820 bp of central region of *omcS* was cloned to the plasmid. The constructed plasmid was first introduced into *Escherichia coli* S17 strain, which further conjugated with *G. sulfurreducens* CL1 strain. All *G. sulfurreducens* colonies grew anaerobically on NBAF agar plate under 30 °C. A single-step recombination occurred between plasmid gene and genomic *omcS* with the constant supply of 200 μg ml^{-1} kanamycin, which could disrupt the genomic *omcS.* Successful disruption was confirmed by PCR and nanowire preparation.

Author Manuscript Author Manuscript Author Manuscript Author Manuscript

OmcZ nanowire purification

The CL1 *omcS:pk18* strain was grown anaerobically in 10 l NBAF medium. Cells reaching the stationary phase were collected by centrifugation and the cells were homogenized in 150 mM ethanolamine (ETA) buffer. Then nanowires were collected by blending for 2 min at a low speed. The mixture was then subjected to 8,000*g* centrifugation for 10 min to remove the cell debris. The supernatant containing nanowires was subjected to ultracentrifugation at 100,000*g* for 1 h to pellet OmcZ nanowires. The pelleted OmcZ nanowires were further resuspended in the appropriate amount of 15 mM pH 10.5 ETA buffer and loaded for sucrose gradient. The sucrose fractions were loaded accordingly with the following formula without the disturbance between each layer, and all the sucrose solutions were made with 15 mM pH 10.5 ETA:

2 ml 60% sucrose, 7 ml 50% sucrose, 12 ml 40% sucrose and 12 ml 30% sucrose.

No more than 600 μl of OmcZ sample was mixed with 20% sucrose to the final volume of 2 ml and layered on top of the gradient. The tube was then loaded to SW 32 Ti swing-bucket rotor (Beckman) and ultra-centrifuged at 100,000*g* overnight (>16 h). After ultracentrifugation, most OmcZ nanowires would stay at the density of ~30% to form a red ring. The red ring containing OmcZ nanowires was gently separated from the rest of the solution, and the sucrose was removed either through dialysis or buffer exchange against 15 mM ETA buffer. To further remove small protein contaminations, the sample was loaded to a gel filtration column packed with Sephacryl 500-HR resin (Cytiva) and OmcZ nanowires were collected at ~0.4–0.5 fraction of the volume. The final sample was concentrated and stored in 15 mM ETA buffer at pH 10.5. The sample purity was assessed by both Coomassie blue and haem staining.

Cryo-EM sample preparation conditions for OmcZ

A total of 0.125 M urea was added to the OmcZ sample 1 h before the sample preparation to disperse the OmcZ nanowires. Three-hundred mesh C-flat grids were first glow discharged with air inflow for 20 s, and then 4 μl of the sample was cast on the grids. The grids were then transferred to an FEI Vitrobot Mark IV operating at 22 °C with 100% humidity and blotted for 4 s with the force strength of 2 and plunge frozen in liquid ethane.

OmcZ data collection

Frozen grids were imaged on Titan Krios G3i+, operating at 300 kV equipped with a K3 detector (Gatan). Micrographs were recorded with super-resolution mode at 0.828 Å per pixel, with a total dose of ~60 e^{-} $Å^{-2}$ fractioned into 50 frames. A defocus range of 1–2.5 μm was used to collect ~14,500 images in total. Quantum energy filter with a slit width at 20 eV was applied to remove inelastically scattered electrons.

OmcZ data processing

All movies were first motion corrected with MotionCorr implemented in RELION 3.0.8 (ref. [52]) using all the frames. The contrast transfer function was estimated using GCTF v1.10 (ref. [53]). The particles were first manually picked to generate a reliable 2D classification, which was then used as the matching templates for auto picking implemented in RELION.

Author Manuscript Author Manuscript Author Manuscript Author Manuscript

Approximately 900,000 particles were selected with the box size of 384 pixels, and after 2D classification, ~280,000 particles were selected. All ~280,000 particles were first used to generate a 3D map by imposing the helical symmetry (helical rise ~57 Å, helical twist ~160°), and a featureless cylinder was used as a starting reference. The consensus map was then used as the reference to run 3D classification ($K = 4$) and final ~120,000 particles were combined and used for another round of refinement. Subsequent contrast transfer function refinement and Bayesian polishing improved the resolution to 3.5 Å (gold standard), where protein backbone and haem positions became evident and ready for model building.

OmcZ model building

The density map was first segmented using volume segmentation in Chimera 1.15 (ref. [54]) and the backbone of the monomer was manually traced against the density using Baton mode implemented in Coot. All eight haem molecules are manually placed into the density and adjusted in Coot with the haem geometry imposed. All the thioether bonds and the histidine coordination were manually created in PDB files and fixed for the downstream refinement. The monomer coordinates were firstly refined in Phenix with defined haem geometry and ideal bond length for the covalent bonds attached to the haems. The refined monomer coordinate was then expanded into trimers and the trimmer model was further refined in Phenix with NCS operator and imposed haem geometry. The refined model was further manually inspected and corrected in Coot. Then the model was subject to another round of real space refinement in Phenix, and the final model was selected based on the lowest MolProbity score.

Conservation map calculation

Conservation of the residues was calculated using the Consurf Server[55] and the PDB structure of monomeric OmcZ was used as a user-provided input. The homologous proteins of OmcZ were searched using HHMER against the Uniref90 database. The output result was further rendered in Chimera X[56].

Purification of OmcS nanowires from *G. sulfurreducens*

OmcS nanowires were obtained from *G. sulfurreducens* strain[29] CL-1 and nanowires were purified as described previously[50].

CD

Samples containing OmcS or OmcZ was first dialysed into 15 mM ETA buffer. The protein concentration was determined using both bicinchoninic acid assay and ultraviolet–visible (UV–vis) spectroscopy using the previously published extinction coefficient. CD scans of protein and buffer background were collected between 350 and 480 nm with a 1 mm or 2 mm path length quartz cuvette using a spectrometer (Chirascan, Applied Photophysics). Each buffer or protein sample was scanned with three replicates. All replicate spectra were averaged, and the averaged buffer background was subtracted from all averaged nanowire spectra. To convert the raw ellipticity values (millidegrees (mdeg)) to molar ellipticity values ((θ); deg cm^2 $dmol^{-1}$), the following formula was used:

Author Manuscript Author Manuscript Author Manuscript Author Manuscript

$$\theta = \frac{\text{mdeg} \times \text{MW}}{l \times C}$$

where MW is the mean residue weight, l is the path length of the cuvette in centimetres and C is the concentration of the protein in mg ml^{-1}.

Molecular dynamics simulation for relaxing structures used in CD spectral computations

System setup and parameterization: Starting from the cryo-EM structure of an OmcZ nanowire (PDB accession code: 7LQ5), a trimer model was constructed from chains A, B and C. Each of these chains contains eight *c*-type, bis-histidine-coordinated haem co-factors, which were modelled in the oxidized (formal Fe(III) centre) state.

The trimer model has 45 Asp, 12 Glu, 51 His (only three of which are not coordinated to the iron centre of a haem co-factor), 21 Lys, 12 Arg and 12 Tyr residues that are titratable. These residues were assigned standard protonation states (for example, deprotonated Asp and Glu; singly protonated His; protonated Lys, Arg and Tyr) to simulate circumneutral pH conditions.

Using tLEaP in the AmberTools20 package[57,58], hydrogen atoms were added to the trimeric OmcZ structure assuming standard or full protonation of titratable residues. The structure was placed at the centre of a box of explicit water with at least a 15 Å buffer region to the boundary of the box. A sufficient number of counterions (45 Na^+ at circumneutral pH) was added to achieve charge neutrality. Standard proteinogenic residues were modelled with the AMBER FF99SB force field[59]. Parameters for the haem co-factor were adopted from Crespo et al.[60] and Henriques et al.[61], and used as in previous studies for single- and multi-haem systems[62,63]. The TIP3P water model[64] and the monovalent ion parameters of Joung and Cheatham[65] were used to model the solution state.

Pre-production simulations: The trimeric OmcZ structure was subjected to 20,000 steps of steepest descent, followed by a maximum of 100,000 steps of conjugate gradient minimization. A 10 kcal per mol $Å^2$ restraint was applied to the heavy atoms of the protein backbone, as well as selected atoms (PDB names FE, NA, NB, NC, ND, C3D, C2A, C3B, C2C, CA and CB) of each haem group during the minimization. The system was subsequently heated from 0 to 300 K at a rate of 0.3 K ps^{-1} in the constant amount, volume and temperature (NVT) ensemble and held at the final temperature for 1.0 ns. The restraints on the protein backbone and haem groups were reduced to 1.0 kcal per mol $Å^2$ for the heating stage. These restraints were further reduced to 0.1 kcal per mol $Å^2$ for a subsequent 4.0 ns simulation at 300 K and 1 bar in the NPT ensemble to equilibrate the density of the system. This protocol was applied to prepare for the production-stage simulation under circumneutral pH conditions.

All NVT and NPT simulations (including the production-stage trajectories described below) employed periodic boundary conditions, the particle Mesh Ewald[66] treatment of electrostatic interactions with a direct sum cut-off of 10.0 Å, the SHAKE algorithm[67,68] to rigidify bonds to hydrogen atoms, a Langevin thermostat with a collision frequency of 2.0 ps^{-1},

Author Manuscript Author Manuscript Author Manuscript Author Manuscript

and an integration timestep for the Langevin equation of motion of 2.0 fs. Pressure in NPT simulations was regulated with a Monte Carlo barostat having a relaxation time of 1.0 ps. Particle mesh Ewald molecular dynamics in its central processing unit and graphics processing unit[69] implementations in the Amber20 package[58] was used to perform the minimization and dynamical simulations, respectively.

Conventional (unbiased) production-stage simulations: The simulation at circumneutral pH were propagated for 72 ns, respectively, with conventional (unbiased) molecular dynamics in the NVT ensemble at 300 K. The above-mentioned protocol was also used to prepare a structural model of OmcS for comparison in the CD simulations.

CD spectra simulations

CD spectra were computed for the core of haem co-factors in OmcS and OmcZ. It is presently not possible to include more than a fraction of the entire protein at the DFT level of computation, and doing so actually worsens agreement with experiment (preliminary data not shown). The geometry of the haems was taken from the last frame of the production stage molecular dynamics simulation. We use a single frame to approximate the ensemble average that should ideally be used to compute the CD spectra because the geometry of the haem core was largely invariant under thermal fluctuations (that is, no large-scale protein motions occurred to appreciably change the distance and orientation of the haem co-factors).

For each haem in the trimeric models of OmcS and OmcZ, the C_α-C_β bonds of the ligated histidine residues were cleaved, and the dangling bonds were capped with hydrogen atoms to give bis-methylimidazole ligated co-factors. The C_β-S bond of the thioether linkages to the haems were similarly each cleaved and replaced with a capping hydrogen atom.

The CD spectra for these multi-haem systems were modelled at the time-dependent (TD)-DFT level using the B3LYP[70,71] functional and def2-SVP[72] basis set for haems in the reduced (closed shell singlet) state. The reduced state was chosen because (1) the experimental sign-pattern of the CD spectra for OmcS and OmcZ was very similar in both oxidation states, and (2) the problem of spin contamination for open-shell species with TD-DFT[73] was avoided.

The CD spectra were computed using the fragment-based excitonic model[74,75] implemented in Gaussian 16 Rev. A.03 (ref. [76]) and analysed with the Excitonic Analysis Tool[77-79]. The lowest two excited states with an energy no lower than 3.05 eV (406 nm) were computed for each co-factor. literature precedents[80] with TD-DFT calculations on haem systems revealed that the Soret transitions of interest for the CD analysis were always blue-shifted relative to experiment and reside in the 380–400 nm region. A plethora of low-intensity (probably spurious charge transfer) states were typically computed at lower energies (longer wavelengths). The number of excited states considered for each co-factor needed to be restricted for computational tractability because the excitonic model considers systematically the (Coulombic, overlap and exchange correlation) interactions between the transition densities for each excitation on every fragment. There are 18 or 24 haems in the OmcS and OmcZ models, respectively, giving a total of 612 or 1,104 evaluations of the interactions between transition densities on pairs of haems.

Author Manuscript Author Manuscript Author Manuscript Author Manuscript

In comparing theory with experiment, it is important to note: (1) Interactions of the haems with the aqueously solvated protein environment have been entirely neglected. Intensity may be redistributed among the excitations in the presence of these interactions. Simulated intensity is also dependent on the chosen approximate DFT functional[81], but we found no difference in the spectra when using B3LYP or CAM-B3LYP. (2) Simulated wavelengths are expected to be blue-shifted relative to experiment because vertical electronic (not 0–0 vibronic) transitions were computed, and inaccuracies exist in available DFT functionals. The blue shift of the theoretical versus experimental spectra for OmcS and OmcZ was an acceptable ~0.06 eV (ref. [82]) and consistent with literature on haem systems[80]. Remarkably, the different sign patterns in the CD spectra for OmcS and OmcZ were found to be encoded in the haem arrangement alone (Extended Data Fig. 4d). These sign patterns result from haem-haem interactions, because the rotatory strength of a single haem group due to the relative orientation of the axial histidine ligands is minimal.

For more insight into the nature of haem–haem interactions responsible for the spectral differences, we analysed the evolution of the CD spectrum for OmcS and OmcZ as adjacent haems were sequentially added to the computations (Extended Data Fig. 4e). The optical response in the computed CD spectra only results when multiple haems are present, indicating the effect of haem–haem interactions. Differences between the simulated spectra of OmcS and OmcZ emerge with including as few as three haems in the computations.

Notably, the simulated spectra for OmcS and OmcZ were similar when six haems are present in the computations. This result for OmcZ is independent of which six of the eight haems are selected (Extended Data Fig. 4f). A substantial change in the simulated CD spectrum was found when a seventh haem (either the mainchain haem II or branched haem VI) was added to the computations. The addition of an eighth haem does not have an appreciable effect on the sign pattern. Thus, unique interactions specific to an assembly of seven haems are responsible for the different sign patterns between the simulated spectra for OmcS and OmcZ.

Substrate reduction test

All the substrates were freshly made in 20 mM Bis-Tris buffer at pH 7.2 followed by 1 h of degassing using a pure N_2 gas to scavenge the oxygen. Iron oxide reduction was performed using freshly precipitated β-FeO(OH) (akaganite) (110 mM). The Fe(III) concentration was measured with a ferrozine assay.

Reduction and oxidation of the cytochromes were monitored by UV–vis spectroscopy using a 1 cm path length cuvette. Briefly, 5 μM of OmcZ or OmcS sample was first dialysed into 20 mM Bis-Tris buffer at pH 7.2. Dialysed samples were then reduced with 10 mM of DTT in an anaerobic chamber overnight. Q bands are the UV–vis absorption of porphyrins observed in the range 500–750 nm, and their splitting corresponds to α- and β-bands[34]. The α-band is commonly used to monitor substrate reduction[34]. The successful reduction was confirmed by UV–vis spectra showing the splitting of Q band with no further change over time. The excessive amount of the substrate of substrates (final concentration ~1 mM) was directly added to the reduced nanowire samples. Upon addition, the UV–vis spectra were recorded in a timely manner. The recording stopped after a complete diminish of splitting of

Author Manuscript Author Manuscript Author Manuscript Author Manuscript

Q band. Control was made with degassed buffer to ensure no random oxidation happening within the period.

To calculate the area of α-band, the area under the curve between wavelength 543 nm and 562 nm was first calculated by integration. Then the baseline area was calculated by first fitting a straight line between these two wavelengths and the area was integrated under the line[33]. Then the area of α-band was finally calculated as the difference between these two areas. The calculation was repeated for each timepoint, and all the calculations were implemented as a single Python script for automation.

Stability experiments

Purified OmcZ nanowires were subjected to adding denaturants to the final concentration of 6 M urea, 5 M GuHCl, 2% SDS and phosphoric acid at low pH (pH 1.6) respectively and incubated at room temperature overnight. Their stability was assessed by negative-stain TEM, CD spectroscopy and UV–vis spectroscopy (Extended Data Fig. 6). In addition, visual inspection confirmed that the red colour due to haems was retained under all denaturants.

Purification of $OmcZ_{50}$ from *G. sulfurreducens*

$OmcZ_{50}$ were obtained from *G. sulfurreducens* strain CL1-*ΔomcS*. Twenty litres of culture was grown until OD_{600} ~0.6, and the cells were collected via centrifugation. Then periplasmic fraction was extracted following the previous established protocol[30]. The periplasmic fraction was then loaded to a gel filtration column embedded with 500 S-HR Sephacryl resin (Cytiva) and running in 40 mM Tris buffer with 250 mM sucrose. The sample with peak corresponds to the non-filamentous form of OmcZ was combined and ran through an anion exchange column. The majority of $OmcZ_{50}$ did not bind to the column and was collected in the flow-through. Then the sample was further loaded to 200 high-resolution columns for purification. The sample with peak corresponds to a non-filament form of OmcZ was combined, and $OmcZ_{50}$ was the only OmcZ protein confirmed by western blot.

Expression and purification of $OmcZ_{50}$ in *E. coli*

A piece of genomic DNA coding for *omcZ* (*gsu2076*), *ozpA* (*gsu2075*) and prolyl isomerase (*gsu2074*) was amplified with Phusion DNA polymerase (Thermo Fisher) and primers OmcZ-F and 2074-R (Supplementary Table 2). Then the backbone of plasmid pCK32 (ref. [83]) was amplified with primers Vec-F and Vec-R (the amplified backbone included everything but the *ppcA* gene). The two PCR fragments were assembled with In-Fusion HD cloning kit (Takara Bio). The resulting plasmid was named pOmcZ-3.

Next, this plasmid was mutated to shorten the second haem-binding motif, which is non-conventional and required modification for the expression in *E. coli.* It was amplified with primers D12-F and D12-R, and the PCR product (the entire plasmid except for 36 bp in the haem-binding motif) was re-circularized with the same cloning kit. The resulting plasmid was named pOmcZ-4.

Author Manuscript Author Manuscript Author Manuscript Author Manuscript

Finally, pOmcZ-4 was mutated to insert the Strep-tag II[84] at the very C-terminus of OmcZ. The plasmid was amplified with primers Str-F and Str-Rev and the PCR product was re-circularized in the same way. The new plasmid was named pOmcZ-9.

All plasmids were verified by sequencing at Keck Sequencing Facility, Yale University.

E. coli strain BL21 was used for all experiments. To express $OmcZ_{50}$ in *E. coli,* the frozen stock containing cytochrome maturation machinery[85] was transformed with pOmcZ-9 and then streaked on the plate supplied with both ampicillin (50 μg ml^{-1}) and chloramphenicol (37 μg ml^{-1}) and grew overnight at 37 °C. A single colony was picked and transferred to a small Terrific Broth culture (50 ml) with both antibiotics and cultured at 30 °C with ~150 r.p.m. shaking overnight (~16 h). The pre-culture was then transferred to a 6 × 2 l large Terrific Broth culture with 1:100 dilution and was first cultured to maximum OD (~5) with normal shaking speed (~110 r.p.m.) (~12 h) and then reduced to a lower shaking speed (~65 r.p.m.) and cultured for another 24 h for induction without any inducer.

To purify the protein, the cells were first pelleted by centrifugation (12,000*g*, 10 min) and the cells were lysed by sonication with 50 mM Bis-Tris buffer (pH 7.2) and 250 mM sucrose. Then the soluble lysate was separated from the insoluble part by ultracentrifugation (100,000*g*, 1 h). The soluble lysate was loaded to a Strep Trap XT column (Cytiva) and the bound protein was eluted with the gradient of biotin buffer (up to 50 mM) prepared in 40 mM ETA buffer with the addition of 250 mM sucrose. $OmcZ_{50}$ was then subject to gel filtration (Superdex 200 Increase HiScale 16/40, Cytiva) to further purify the sample.

OzpA expression and purification

OzpA gene and *gsu2074* were cloned as one amplicon from pOmcZ-9 and an N-terminal StrepII tag and flexible linker with TEV cleavage site were added to *ozpA* while a 6× His tag was added to the C-terminus of *gsu2074.* Briefly, *ozpA* and *gsu2074* was amplified with primers 20745_his_F and 20745_his_R (Supplementary Table 3). The backbone of pOmcZ-9 plasmid (without OmcZ, OzpA and GSU2074) was amplified with primers P_F and P_R. The signalling peptide of OzpA is fused to a StrepII tag with a flexible linker attached to a TEV cleavage site and it was directly synthesized as a DNA oligo with the sequence (5′-ATGAGGTATCTGCTCGCCGTTACGGCTCTTTTTATCCT GCTGCCTCCTCTGGGTGACGCTTTTGCCTGGAGCCATCCGCAATTT GAGAAGAATTCGAGCTCGAACAACAACAACAATAACAATAACAACAAC GAAAACCTGTACTTCCAGGGT -3′) and the overhang was added by PCR with primers TEV_strep_F and TEV_strep_R. All the fragments with the plasmid backbone were assembled to the expression plasmid by Gibson assembly.

The constructed plasmid was first transformed into *E. coli* DH5α strain and streaked on an LB plate with ampicillin. The correct construct was verified by sequencing.

E. coli BL21 expression strain was transformed with the plasmid containing the correct insertion of *ozpA* and gsu2074 with the supply of 200 μg ml^{-1} of ampicillin. The expression condition was first screened with different concentrations of isopropyl-β-D-thiogalactoside (IPTG) as the inducer and two different growing temperatures (20 °C and 30 °C). On the

Author Manuscript Author Manuscript Author Manuscript Author Manuscript

basis of the screening result, 50 μM of IPTG with the induction temperature at 20 °C was used for downstream expression.

For expression, the frozen stock of BL21 strain with the correct plasmid was first streaked on the LB plate with ampicillin. A single colony was picked and subcultured at 30 °C overnight until confluent. Then the subculture was diluted 1:100 into three bottles of 2 l LB medium containing 200 μg ml^{-1} ampicillin and grew at 30 °C with shaking at 110 r.p.m. 50 μM of IPTG was added once the OD reached ~1.8, and the temperature was lowered to 20 °C and induced overnight.

For purification of OzpA, the cells were first spun down at 10,000*g* and lysed in 40 mM Tris buffer at pH 7.5 with 50 mM of sodium chloride via a microbial fluidizer. The soluble part of the lysate was separated from the insoluble by ultracentrifugation at 100,000*g* for 45 min. The soluble lysate was loaded onto FPLC with a 5 ml StrepTrap XT column (Cytiva). The bound protein was eluted with a gradient of biotin up to 50 mM. The majority of the eluted proteins precipitated overnight, and the soluble part was separated from the insoluble by centrifugation. The soluble protein was then subject to gel filtration column to further purify the premature OzpA and dialysed against 20 mM sodium phosphate buffer (pH 7.2).

Premature OzpA underwent auto-maturation at room temperature overnight as seen in other subtilase[86]. The mature protein was further purified via anion exchange column (HiTrap Q FF, Cytiva) and the purified mature protein was confirmed by SDS–PAGE gel and mass spectrometry.

In vitro digestion of $OmcZ_{50}$ for self-assembly test

Nine microlitres of purified $OmcZ_{50}$ (~10 μM) was incubated with 1 μl of purified OzpA enzyme (0.5 mg ml^{-1}) overnight at the room temperature. The digestion of $OmcZ_{50}$ was confirmed by western blot or haem staining and the self-assembled OmcZ nanowires were confirmed by TEM and immunogold labelling as previously described[10] using two different peptide antibodies targeting $OmcZ_{30}$ and $OmcZ_{50}$ specifically. Both antibodies were synthesized by LifeTein by immunizing rabbits with synthetic peptide sequence ($OmcZ_{30}$: DSPNAANLGTVKPGL; $OmcZ_{50}$:KTINGPLSGKILAAPKKVKR).

Negative-stain TEM

CF400-CU grids were first plasma cleaned at low power setting for 40 s, and the samples containing nanowires or bacteria were drop cast on the grids and absorbed to the grids for 5 min. Then the excess liquid was removed by filter paper, and then the grids were floated on top of 50 μl droplet of 1% phosphotungstic acid (pH adjusted to 7) with the carbon side facing the liquid and stained for 2 min for protein sample or 30 s for bacterial sample. Then the excessive stain was removed by filter paper and the grids were allowed to be air dried before checking under TEM. TEM images were taken with JEM-1400 series (JEOL) microscope located on Yale West Campus with 80 kV operating voltage.

Author Manuscript Author Manuscript Author Manuscript Author Manuscript

Power spectrum analysis

TEM images with the same pixel size were used for power spectrum analysis. e2helixboxer.py implemented in EMAN2 (ref. [87]) was used for picking particles along the nanowires. The boxed nanowires were further segmented into particles with 384 pixel size in SPRING[88]. The averaged power spectrum was generated based on the picked particles by using segmentexam implemented in SPRING.

AlphaFold prediction of OmcZ and OzpA structure

AlphaFold suite[40,89] was downloaded and installed from https://github.com/deepmind/alphafold. For the prediction of OmcZ, the sequences were downloaded from the National Center for Biotechnology Information (GenBank ID: MRG77204.1 and CAG1009295.1). The signalling peptide was predicted by SignalP 6.0 online server and removed from the sequence based on the prediction. Then the sequences were used as input for AlphaFold prediction, and five models were generated for each sequence and the top-ranked models, based on the model confidence generated by the program[89], were used for all the subsequent analysis. Haems were then manually built inside the model structure based on the predicted haem binding motifs and a trimer model was built for each monomer structure. The haem arrangement in the models was obtained based on the position of cystines and histidines that form haem binding motif. A pymol command 'pair_fit' was used to insert haems in the AlphaFold structure that showed a good agreement with the cryo-EM structure. The root-mean-square deviation score was computed using the Local–Global Alignment method[90] from the online server AS2TS http://linum.proteinmodel.org/.

For the prediction of OzpA and OmcZ multimer, annotated catalytic domain of OzpA from Uniprot was used as input sequence for OzpA, and the full sequence of OmcZ without the signalling peptide was used as the input for OmcZ sequence. Then the multimer structure was predicted using AlphaFold multimer suite[89]. Out of five predicted models, the top-ranked model was used for figure generation and interpretation. RNA structure of the intergenic region of mRNA between omcZ and ozpA was modeled using ViennaRNA suite Package 2.094.

Phylogenetic tree

OmcZ homologues were searched via protein basic local alignment search tool, and the top 100 hits were downloaded from the National Center for Biotechnology Information. The alignment of OmcZ homologues was performed in MEGAX[91] using the MUSCLE algorithm[92]. Then the aligned sequences were further used to generate phylogenetic tree in MEGAX using maximum likelihood approach with bootstrap. The final tree was visualized and rendered in web-based Interactive Tree of Life[93].

RT–PCR

Log-phase WT *G. sulfurreducens* cells (OD 0.5) were used for RNA extraction. The cells were collected by centrifugation at 4,000 r.p.m. for 5 min from 5 ml of cell-containing medium. The pellet was resuspended in 200 μl of lysis buffer (100 mM Tris, 1 mM EDTA, 20 mg ml^{-1} proteinase K and 1 mg ml^{-1} lysozyme) in a 1.5 ml Eppendorf tube by pipetting. The tube was vortexed for 10 s and then incubated at room temperature for 10 min with a

Author Manuscript Author Manuscript Author Manuscript Author Manuscript

vortex every 2 min. After lysis, the total RNA was extracted, and clean-up was performed using RNeasy Mini Kit (Qiagen) following the instructions provided by the manufacturer.

Complementary DNA was obtained by reverse transcribing ~200 ng clean RNA using superscript II kit with random primers. The control cDNA was generated using the same protocol without adding the reverse transcriptase. Then the cDNA was used as the template to amplify the intergenic region between *omcZ* and *ozpA* using a forward primer (5′-CCAGCCCGGACTTTGCAACCAA-3′) and a reverse primer (5′-CGCCGTGCCGATAGACCTTCTC-3′). The expected size of the PCR product is 373 bp and was visualized on the 1% DNA agarose gel.

Native mass spectrometry for haem quantification

The proteins were buffer exchanged to 200 mM ammonium acetate (MP Biomedicals), 2 mM DTT with Zeba Spin Desalting Columns (Thermo Fisher Scientific). The protein concentration in the analysed sample was ~5 μM. OmcZ nanowires purified from *G. sulfurreducens* was monomerized by boiling in SDS and used as a positive control. Native mass spectrometry was performed on Q Exactive UHMR (Thermo Fisher Scientific) using in-house nano-emitter capillaries. The tips in the capillaries were formed by pulling borosilicate glass capillaries (outer diameter 1.2 mm, inner diameter 0.69 mm, length 10 cm; Sutter Instruments) using a Flaming/Brown micropipette puller (ModelP-1000, Sutter Instruments). Then the nano-emitters were coated with gold using rotary pumped coater Q150R Plus (Quorum Technologies). To perform the measurement the emitter filled with the sample was installed into Nanospray Flex Ion Source (Thermo Fisher Scientific). Mass spectrometry parameters for the analysis of the proteins include spray voltage 1.5 kV, capillary temperature 275 °C, resolving power 3,125 at *m/z* of 400, ultrahigh vacuum pressure 4.6×10^{-10} torr to 8.18×10^{-10} torr, in-source trapping between 100 V and 200 V. Data were visualized with the Xcalibur software and assembled into figures using Adobe Illustrator.

Using native mass spectrometry, we confirmed that the observed mass for $OmcZ_{50}$ is consistent with the successful incorporation of all eight haems and $OmcZ_{50}$ tends to dimerize. However, haem incorporation varied, probably due to differences in the cultures. Therefore, we validated haem incorporation for each culture. Then we performed the same digestion assay in vitro with OzpA on the $OmcZ_{50}$ with eight haems as described above. OmcZ purified from *G. sulfurreducens* was used as a control for the validation of the method.

Immunoblotting and antibody characterization

As described previously[30], custom polyclonal anti-OmcZ antibody was synthesized by LifeTein by immunizing two rabbits with synthetic peptide sequence (DSPNAANLGTVKPGL) containing targeted epitope on the native protein, OmcZ, and then affinity purifying the serum against that peptide sequence. The antibody was used at a dilution of 1:5,000 for immunoblotting. Filament preps were normalized to the initial cell mass of the starting material. Antibodies were designed to target the 30 kDa and 50

Author Manuscript Author Manuscript Author Manuscript Author Manuscript

kDa domains separately, and their specificity was established using either western blot or immunogold labelling.

Statistics and reproducibility

All experiments were performed at least in triplicate and yielded similar results.

Extended Data

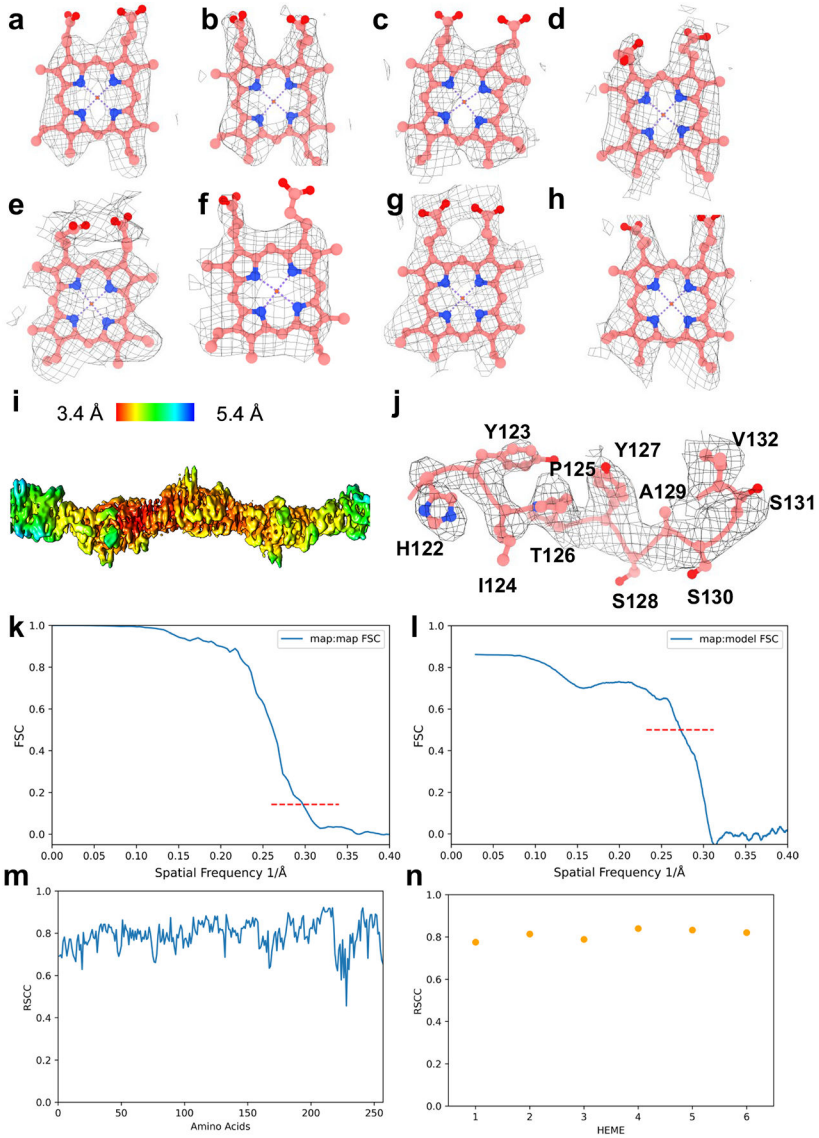

Extended Data Fig. 1 |. Illustration of cryo-EM map quality.

a–g, Density fitting of individual heme cofactors. Low iron density is due to the non-selection of coordinated histidine when rendering the figures at the given threshold of the density. **i**, Resolution distribution of the cryo-EM map. **j**, Representative density of sidechains. **k**, Map to map FSC. **l**, Map to model FSC. **m**, Real space correlation coefficient (RSCC) for each residue. **n**, Heme RSCC.

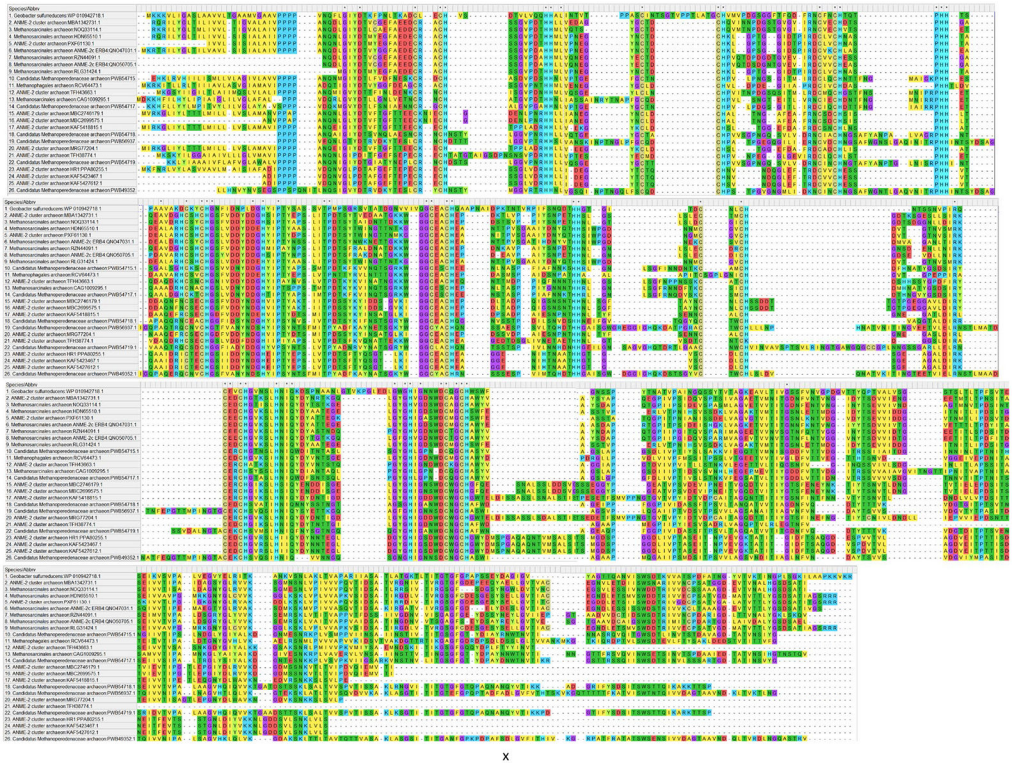

Extended Data Fig. 2 |. *omcZ* homologues show high sequence similarity.

omcZ homologues show up to 68% sequence similarity. In addition to all heme binding motifs, key residues are also highly conserved which we found to be critical for high conductivity. For example, a consecutive pair of histidines that brings T-stacked hemes closer is also highly conserved in all *omcZ* homologs. Thus significant sequence identities are present throughout the protein.

Author Manuscript Author Manuscript Author Manuscript Author Manuscript

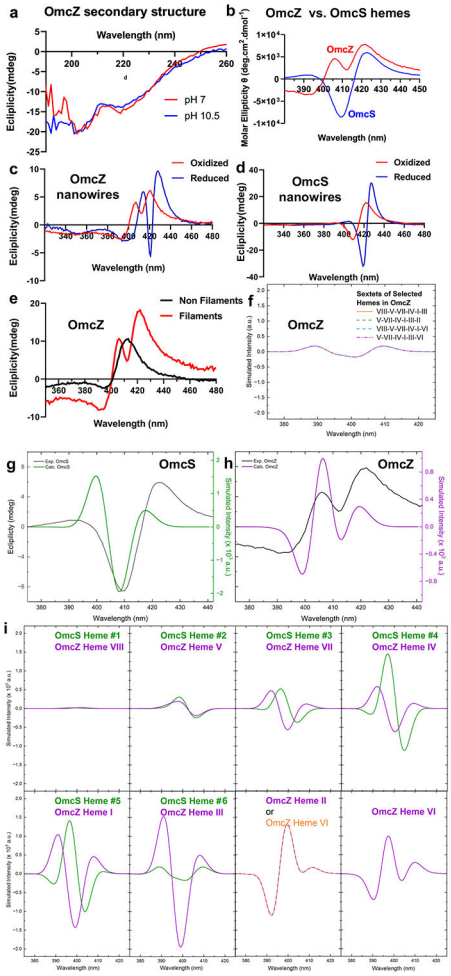

Extended Data Fig. 3 |. Circular Dichroism (CD) spectroscopy shows unique heme arrangements for OmcZ nanowires.

a, CD spectra OmcZ nanowire shows similar secondary structure at pH 10.5 and pH 7 buffer. **b**, CD spectra of OmcS and OmcZ nanowire hemes. Reduced spectrum show narrowing, and a red-shift of the peaks compared to the oxidized spectrum for **c**, OmcZ. **d**, OmcS nanowires as expected. **e**, The double positive peak feature is unique to the OmcZ nanowires, while the non-filamentous $OmcZ_{30}$ fails to show a such feature. **f**, Simulated CD spectra for various sextets of hemes from OmcZ showing that the line shape is independent of six hemes included in the computations. Simulated CD spectra of **g**, OmcS (green) and **h**, OmcZ (pink), using only hemes and heme binding motifs show the peak features observed in the experimental data (black). The simulated spectra were uniformly shifted to longer wavelength by 0.06 eV (see methods for details) **i**, Resolving the contribution of individual hemes to the CD spectra for OmcS and OmcZ reveals that the double peak is a specific feature of hemes in OmcZ nanowires. Evolution of the CD spectra as adjacent hemes in OmcS (green) and OmcZ (pink) were sequentially added to the computations. The labels in each panel indicate which hemes were added for the spectra. The sequence of addition is from left-to-right in both rows.

Author Manuscript

Author Manuscript

Author Manuscript

Author Manuscript

Author Manuscript

Author Manuscript

Author Manuscript

Author Manuscript

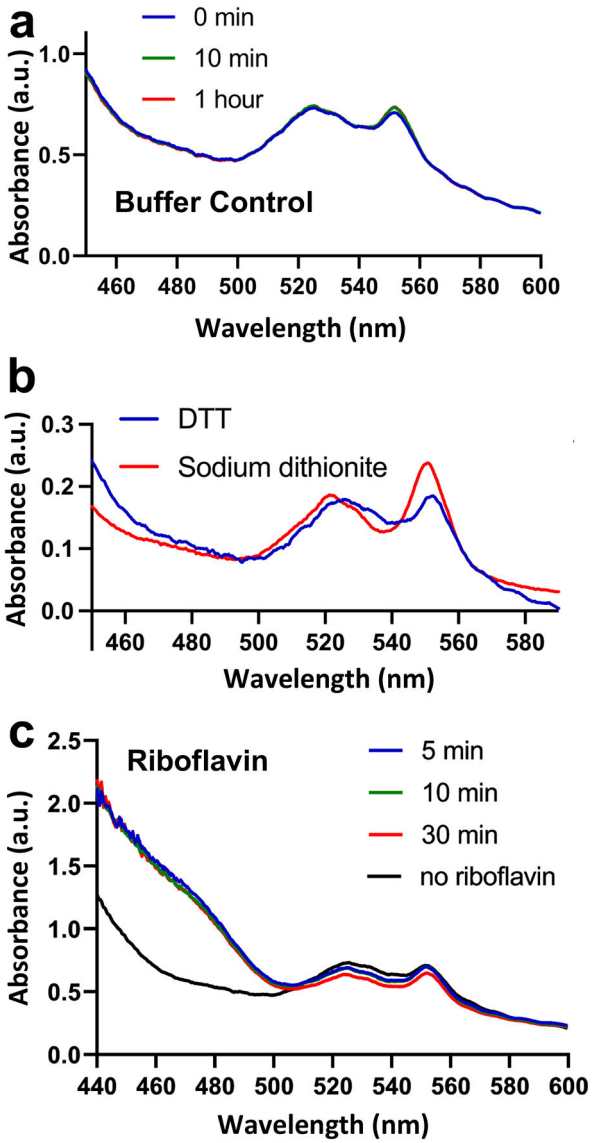

Extended Data Fig. 4 |. OmcZ nanowires reduce diverse electron acceptors.

a, Buffer Control: OmcZ nanowire spectra do not change after 1 hour upon addition of degassed deionized bis-tris buffer (20 mM, pH=7.2) used for all substrate reduction experiments. **b**, OmcZ nanowires could not be fully reduced by DTT but could be reduced by Sodium dithionite. **c**, OmcZ cannot reduce riboflavin.

Author Manuscript

Author Manuscript

Author Manuscript

Author Manuscript

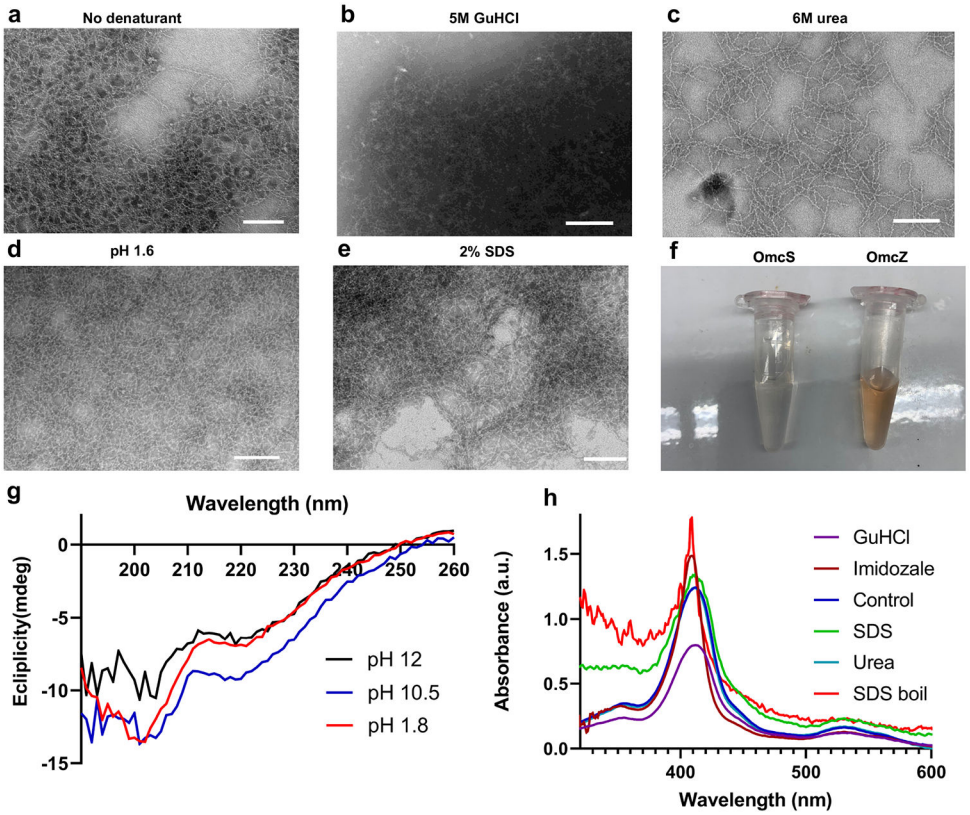

Extended Data Fig. 5 |. OmcZ nanowires are robust electronic biomaterials that function under extreme environments.

Negative staining TEM images of OmcZ nanowires treated with following protein denaturants. **a**, No denaturant. **b**, 6 M urea, **c**, 5 M GuHCl, **d**, Phosphoric acid at low pH (pH = 1.6), and **e**, boiled in 2% SDS. All scale bars: 100 nm. **f**, OmcZ nanowires are more stable than OmcS at low pH (pH = 1.6) as evident by retention of its red colour due to hemes. OmcZ nanowires also retained their red colour characteristic of haems under all other denaturants. **g**, Solution CD spectra and **h**, UV-vis spectra show the stability of protein and electronic structure of OmcZ nanowires in denaturants.

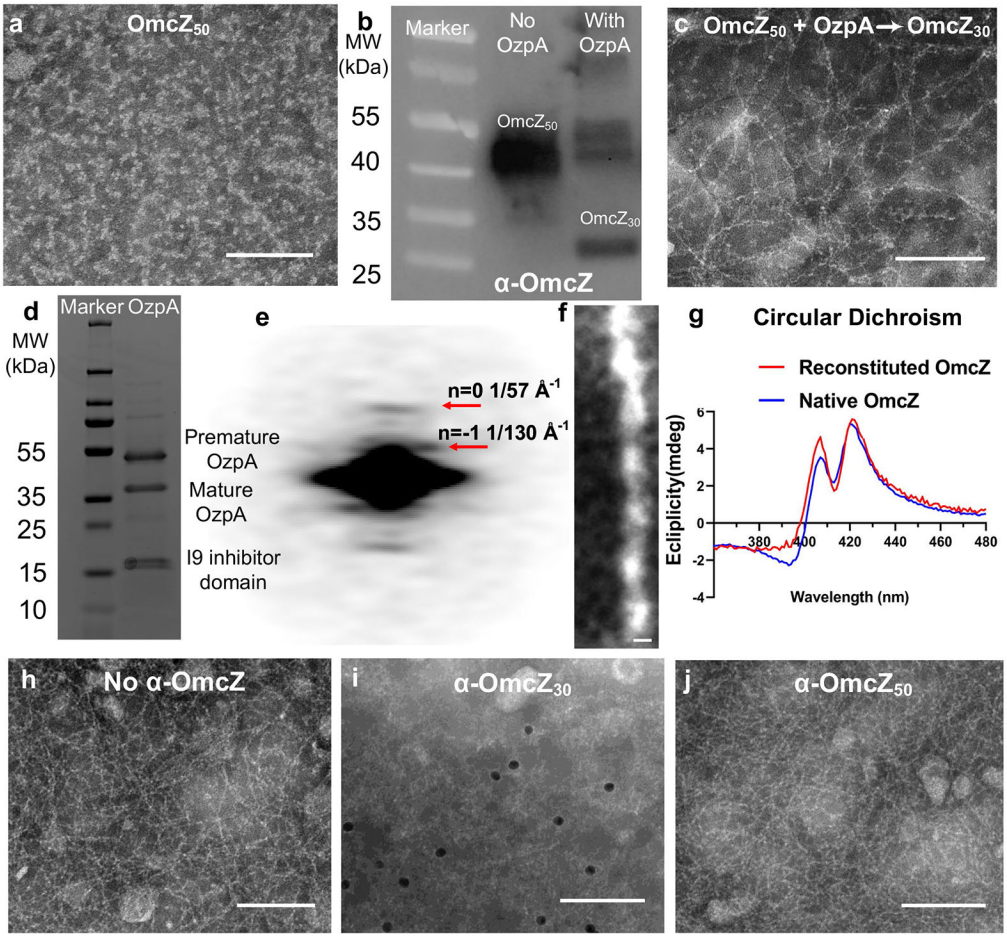

Extended Data Fig. 6 |. *In vitro* Assembly of OmcZ nanowires from native $OmcZ_{50}$.

a, TEM image of native *G. sulfurreducens* $OmcZ_{50}$ showing lack of nanowire assembly. **b**, Western immunoblot using OmcZ antibody showing OzpA digesting $OmcZ_{50}$ into $OmcZ_{30}$. **c**, Digested $OmcZ_{30}$. self-assembles into nanowires *in vitro*. **d**, SDS-PAGE gel of purified OzpA showing three major bands: premature protein, mature protein, and the cleaved inhibitor domain (I9). **e**, Power spectrum of the reconstituted OmcZ nanowires shows the same helical parameters as cell-produced OmcZ nanowires. **f**, 2D average of reconstituted OmcZ nanowires. **g**, CD spectra of reconstituted and native OmcZ nanowires is similar. Immuno-gold labeling of reconstituted OmcZ nanowires using **h**, No-primary antibody, **i**, antibody for $OmcZ_{30}$ and **j**, antibody for $OmcZ_{50}$. Scale bars, **a**, 100 nm. **c**, 50 nm. **c**, 2 nm. **h**, 100 nm, **i**, 50 nm, **j**, 100 nm.

Author Manuscript
Author Manuscript
Author Manuscript
Author Manuscript

Author Manuscript

Author Manuscript

Author Manuscript

Author Manuscript

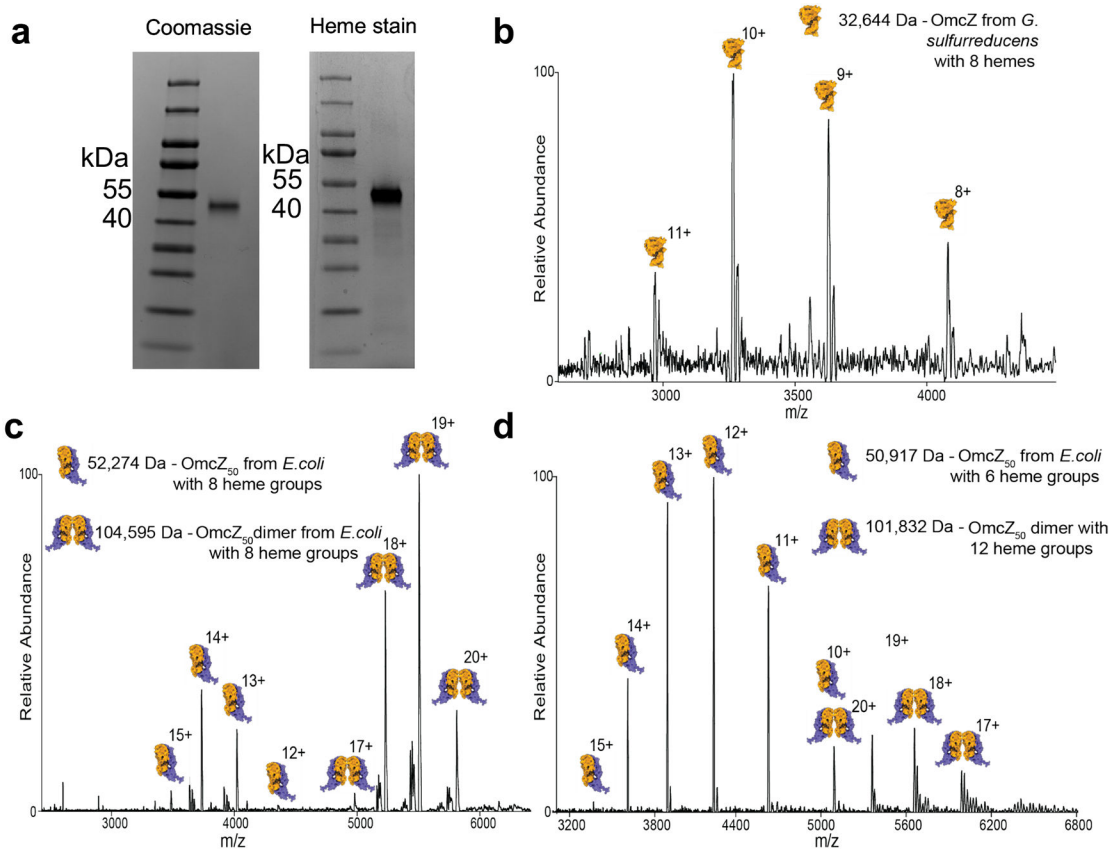

Extended Data Fig. 7 |. Native mass spectrometry of $OmcZ_{50}$ purified from *E. coli* shows molecular weight and heme groups consistent with native $OmcZ_{50}$.

a, Coomassie and Heme staining gel of $OmcZ_{50}$ purified from *E. coli*. **b**, Mass spectrum of OmcZ purified from *G. sulfurreducens*. Detected mass corresponds to the OmcZ monomer covalently bound to eight hemes. **c-d**, Mass spectrum of $OmcZ_{50}$ purified from *E. coli*. Detected proteins exist as monomer and homodimer. Mass analysis shows that $OmcZ_{50}$ monomer is bound covalently to primarily **c**, eight haems but sometimes also to **d**, six hemes.

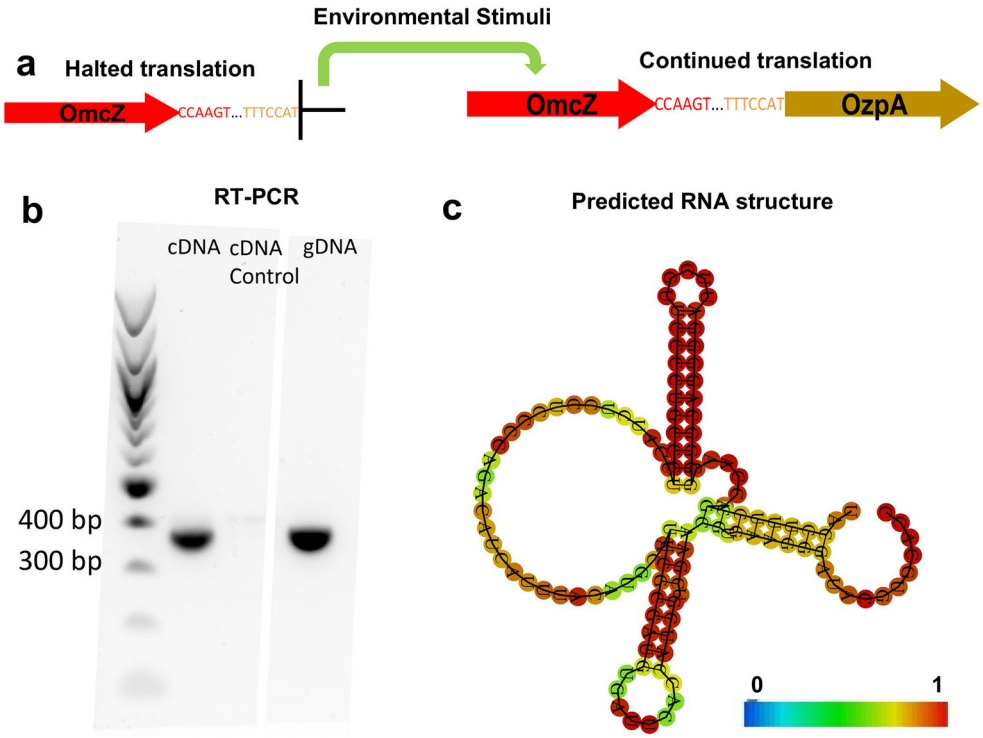

Extended Data Fig. 8 |. OmcZ nanowire assembly could be environmentally controlled.
a, *omcZ* operon genes with intergenic region in *G. sulfurreducens*. **b**, RT-PCR shows that *omcZ* and *ozpA* are co-transcribed. Lanes 1: genomic DNA (gDNA), 2: cDNA, 3: cDNA control. **c**, Predicted RNA structure of the intergenic region of mRNA using ViennaRNA suite. Color code shows the probability of each base or base pair's placement in the secondary structure.

Author Manuscript
Author Manuscript
Author Manuscript
Author Manuscript

Author Manuscript Author Manuscript Author Manuscript Author Manuscript

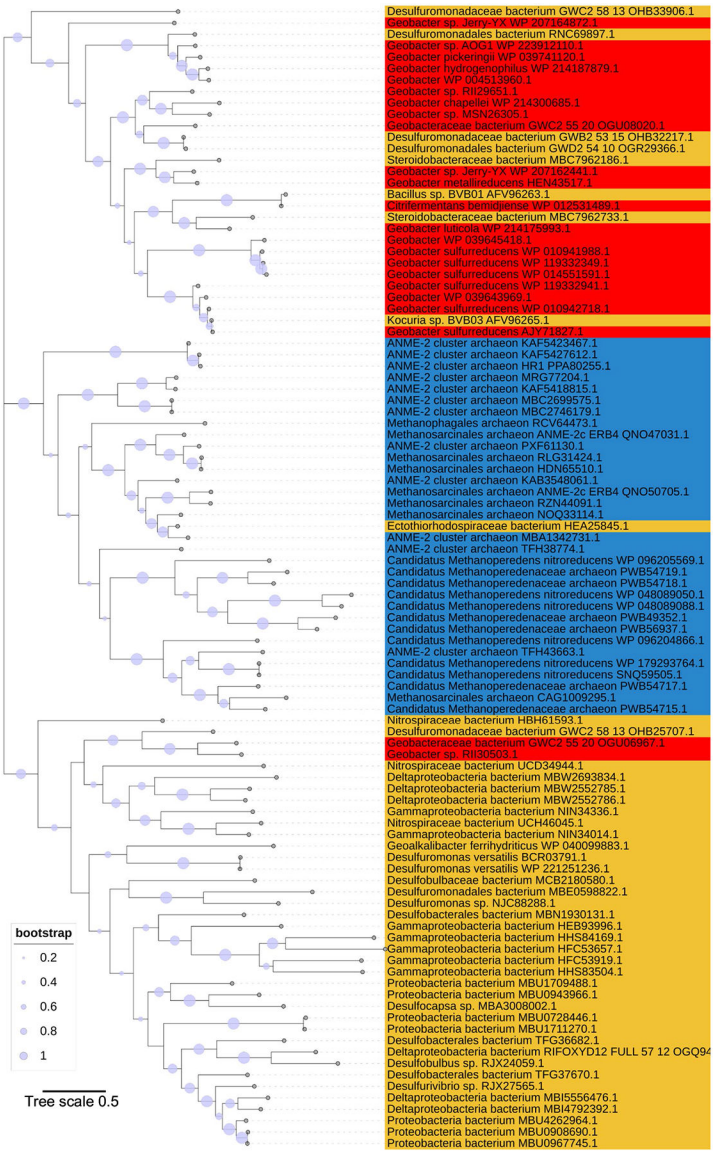

Extended Data Fig. 9 |. *OmcZ* operon is found in diverse microbes.

Phylogenetic tree derived from OmcZ amino acid sequence alignments using homology cut-off score of 100 bit. Light blue circles represent bootstrap values.

Extended Data Table 1 |

Statistics of OmcZ refinement and heme distances

a	OmcZ nanowire (EMD-23481) (PDB 7LQ5)
Data collection and processing	81,000
Magnification (kV)	300
Electron exposure (e-/Å)	50

Author Manuscript Author Manuscript Author Manuscript Author Manuscript

a	OmcZ nanowire (EMD-23481) (PDB 7LQ5)
Defocus range (μm)	1.0-2.5
Pixel Size (Å)	0.828
Symmetry imposed	−159.1 /57.4 Å
Initial particle images (No.)	900,000
Final particle images (No.)	128,000
Map resolution (Å)	3.4
FSC threshold	0.143
Map resolution range (Å)	3.3-5.4
Refinement	
PDB code	7LQ5
Model resolution	3.6
FSC threshold	0.5
Map sharpening B factor	98
Model composition	
Non-hydrogen atoms	6843
Protein residues	774
Ligands	24
B factors	NA
Protein	NA
Ligand	NA
R.m.s deviation	
Bond length (Å)	0.56 (0)
Bond angles (°)	0.64 (0)
Validation	
MolProbity score	2.5
Clash score	26
Poor rotamers (%)	2.6
Ramachandran plot	
Favoured (%)	87.9
Allowed (%)	12.1
Disallowed (%)	0

b	stack	OmcS (Å)	OmcZ (Å)
	T-stack	6.1 ± 0.1	5.1 ± 0.3
	Parallel	4.3 ± 0.3	4.0 ± 0.3

a, Statistics of OmcZ refinement **b**, Hemes in OmcZ are closer than in OmcS as revealed by edge-to-edge distance. Values represent mean ± standard deviation (n = 4 T-stack heme pairs in OmcZ and n = 3 T-stack heme pairs in OmcS, n = 3 parallel-stacked hemes for both OmcS and OmcZ)

Supplementary Material

Refer to Web version on PubMed Central for supplementary material.

Author Manuscript Author Manuscript Author Manuscript Author Manuscript

Acknowledgements

We thank E. Martz for help with structural analysis, C. Shipps for help with UV–vis spectroscopy of reduced OmcZ nanowires, and T. Pollard, M. Hochstrasser and B. Kazmierczak for helpful suggestions. This research was supported by the NSF CAREER award no. 1749662 (to N.S.M.), the NSF EAGER award no. 2038000 (to N.S.M.), the NSF-ANR award no. 2210473 (to N.S.M. and V.S.B.) and the National Institutes of Health Director's New Innovator award (1DP2AI138259-01 to N.S.M. and R01GM141192 to K.G.). Research was sponsored by the Defense Advanced Research Project Agency Army Research Office and was accomplished under Cooperative Agreement Number W911NF-18-2-0100 (with N.S.M. and V.S.B.). High-resolution cryo-EM data collection was performed at the Case Western Reserve University Cryo-Electron Microscopy Core facility with the assistance of Kunpeng Li and Sudha Chakrapani.

Data availability

The key relevant datasets generated during and/or analysed during the current study are publicly available. Cryo-EM data were deposited with the Electron Microscopy Data Bank (ID EMD-23481) and with the Protein Data Bank (ID 7LQ5). Source data are provided with this paper.

References

1. Yalcin SE & Malvankar N The blind men and the filament: understanding structures and functions of microbial nanowires. Curr. Opin. Chem. Biol 59, 193–201 (2020). [PubMed: 33070100]
2. Malvankar NS et al. Tunable metallic-like conductivity in microbial nanowire networks. Nat. Nanotechnol 6, 573–579 (2011). [PubMed: 21822253]
3. Summers ZM et al. Direct exchange of electrons within aggregates of an evolved syntrophic coculture of anaerobic bacteria. Science 330, 1413–1415 (2010). [PubMed: 21127257]
4. Childers SE, Ciufo S & Lovley DR *Geobacter metallireducens* accesses insoluble Fe(III) oxide by chemotaxis. Nature 416, 767–769 (2002). [PubMed: 11961561]
5. Reguera G et al. Extracellular electron transfer via microbial nanowires. Nature 435, 1098–1101 (2005). [PubMed: 15973408]
6. Malvankar NS & Lovley DR Microbial nanowires for bioenergy applications. Curr. Opin. Biotechnol 27, 88–95 (2014). [PubMed: 24863901]
7. Malvankar NS & Lovley DR Microbial nanowires: a new paradigm for biological electron transfer and bioelectronics. ChemSusChem 5, 1039–1046 (2012). [PubMed: 22614997]
8. Wang F et al. Structure of microbial nanowires reveals stacked hemes that transport electrons over micrometers. Cell 177, 361–369 (2019). [PubMed: 30951668]
9. Filman DJ et al. Cryo-EM reveals the structural basis of long-range electron transport in a cytochrome-based bacterial nanowire. Commun. Biol 2, 219 (2019). [PubMed: 31240257]
10. Yalcin SE et al. Electric field stimulates production of highly conductive microbial OmcZ nanowires. Nat. Chem. Biol. 16, 1136–1142 (2020). [PubMed: 32807967]
11. Ye Y et al. Dissecting the structural and conductive functions of nanowires in *Geobacter sulfurreducens* electroactive biofilms. mBio 13, e03822–03821 (2022).
12. Wang F et al. Cryo-EM structure of an extracellular *Geobacter* OmcE cytochrome filament reveals tetrahaem packing. Nat. Microbiol 7, 1291–1300 (2022). [PubMed: 35798889]
13. Gu Y et al. Structure of *Geobacter* pili reveals secretory rather than nanowire behavior. Nature 597, 430–434 (2021). [PubMed: 34471289]
14. Nevin KP et al. Anode biofilm transcriptomics reveals outer surface components essential for high density current production in *Geobacter sulfurreducens* fuel cells. PLoS ONE 4, e5628 (2009). [PubMed: 19461962]
15. Yun J, Malvankar NS, Ueki T & Lovley DR Functional environmental proteomics: elucidating the role of a *c*-type cytochrome abundant during uranium bioremediation. ISME J. 10, 310–320 (2016). [PubMed: 26140532]

Author Manuscript Author Manuscript Author Manuscript Author Manuscript

16. Inoue K et al. Specific localization of the *c*-type cytochrome OmcZ at the anode surface in current-producing biofilms of *Geobacter sulfurreducens*. Environ. Microbiol. Rep 3, 211–217 (2010). [PubMed: 23761253]
17. Chadwick GL, Otero FJ, Gralnick JA, Bond DR & Orphan VJ NanoSIMS imaging reveals metabolic stratification within current-producing biofilms. Proc. Natl Acad. Sci. USA 116, 20716–20724 (2019). [PubMed: 31548422]
18. Peng L & Zhang Y Cytochrome OmcZ is essential for the current generation by *Geobacter sulfurreducens* under low electrode potential. Electrochim. Acta 228, 447–452 (2017).
19. Richter H et al. Cyclic voltammetry of biofilms of wild type and mutant *Geobacter sulfurreducens* on fuel cell anodes indicates possible roles of OmcB, OmcZ, type IV pili, and protons in extracellular electron transfer. Energy Environ. Sci 2, 506–516 (2009).
20. Gaffney EM & Minteer SD A silver assist for microbial fuel cell power. Science 373, 1308–1309 (2021). [PubMed: 34529473]
21. Cao B et al. Silver nanoparticles boost charge-extraction efficiency in *Shewanella* microbial fuel cells. Science 373, 1336–1340 (2021). [PubMed: 34529487]
22. Yi H et al. Selection of a variant of *Geobacter sulfurreducens* with enhanced capacity for current production in microbial fuel cells. Biosens. Bioelectron 24, 3498–3503 (2009). [PubMed: 19487117]
23. Malvankar NS, Tuominen MT & Lovley DR Biofilm conductivity is a decisive variable for high-current-density *Geobacter sulfurreducens* microbial fuel cells. Energy Environ. Sci 5, 5790–5797 (2012).
24. Malvankar NS et al. Electrical conductivity in a mixed-species biofilm. Appl. Environ. Microbiol 78, 5967–5971 (2012). [PubMed: 22706052]
25. Yalcin SE & Malvankar NS Seeing is believing: novel imaging methods help identify structure and function of *Geobacter* nanowires in electricity-producing biofilms in Roadmap on emerging concepts in the physical biology of bacterial biofilms: from surface sensing to community formation. Phys. Biol 18, 051501 (2021).
26. O'Brien JP & Malvankar NS A simple and low-cost procedure for growing *Geobacter sulfurreducens* cell cultures and biofilms in bioelectrochemical systems. Curr. Protoc. Microbiol 43, A.4K.1–A.4K.27 (2017).
27. Malvankar NS, Tuominen MT & Lovley DR Lack of cytochrome involvement in long-range electron transport through conductive biofilms and nanowires of *Geobacter sulfurreducens*. Energy Environ. Sci 5, 8651–8659 (2012).
28. Malvankar NS, Rotello VM, Tuominen MT & Lovley DR Reply to 'Measuring conductivity of living *Geobacter sulfurreducens* biofilms'. Nat. Nano 11, 913–914 (2016).
29. Leang C, Malvankar NS, Franks AE, Nevin KP & Lovley DR Engineering *Geobacter sulfurreducens* to produce a highly cohesive conductive matrix with enhanced capacity for current production. Energy Environ. Sci 6, 1901–1908 (2013).
30. Inoue K et al. Purification and characterization of omcZ, an outer-surface, octaheme *c*-type cytochrome essential for optimal current production by *Geobacter sulfurreducens*. Appl. Environ. Microbiol 76, 3999–4007 (2010). [PubMed: 20400562]
31. Dahl PJ et al. A 300-fold conductivity increase in microbial cytochrome nanowires due to temperature-induced restructuring of hydrogen bonding networks. Sci. Adv 8, eabm7193 (2022). [PubMed: 35544567]
32. Tan Y et al. Synthetic biological protein nanowires with high conductivity. Small 12, 4481–4485 (2016). [PubMed: 27409066]
33. Qian X et al. Biochemical characterization of purified OmcS, a *c*-type cytochrome required for insoluble Fe(III) reduction in *Geobacter sulfurreducens*. Biochim. Biophys. Acta 1807, 404–412 (2011). [PubMed: 21236241]
34. Thirumurthy MA & Jones AK *Geobacter* cytochrome $OmcZ_S$ binds riboflavin: implications for extracellular electron transfer. Nanotechnology 31, 124001 (2020). [PubMed: 31791015]
35. Okamoto A et al. Uptake of self-secreted flavins as bound cofactors for extracellular electron transfer in *Geobacter* species. Energy Environ. Sci 7, 1357–1361 (2014).

Author Manuscript Author Manuscript Author Manuscript Author Manuscript

36. Lovely DR et al. *Geobacter*: the microbe electric's physiology, ecology, and practical applications. Adv. Microb. Physiol 59, 1–100 (2011). [PubMed: 22114840]
37. Fukushima T et al. The molecular basis for binding of an electron transfer protein to a metal oxide surface. J. Am. Chem. Soc 139, 12647–12654 (2017). [PubMed: 28806874]
38. Shapiro D et al. Protein nanowires with tunable functionality and programmable self-assembly using sequence-controlled synthesis. Nat. Commun 13, 829 (2021).
39. Kai A et al. Proteolytic maturation of the outer membrane *c*-type cytochrome OmcZ by a subtilisin-like serine protease is essential for optimal current production by *Geobacter sulfurreducens*. Appl. Environ. Microbiol 87, e02617–e02620 (2021). [PubMed: 33837010]
40. Jumper J et al. Highly accurate protein structure prediction with AlphaFold. Nature 596, 583–589 (2021). [PubMed: 34265844]
41. Tauzin AS et al. Molecular dissection of xyloglucan recognition in a prominent human gut symbiont. mBio 7, e02134–02115 (2016). [PubMed: 27118585]
42. Lovley DR Microbial nanowires. Curr. Biol 32, R110–R112 (2022). [PubMed: 35134353]
43. Chan CH, Levar CE, Jiménez-Otero F & Bond DR Genome scale mutational analysis of *Geobacter sulfurreducens* reveals distinct molecular mechanisms for respiration and sensing of poised electrodes versus Fe(III) oxides. J. Bacteriol 199, e00340–00317 (2017). [PubMed: 28674067]
44. Chadwick GL et al. Comparative genomics reveals electron transfer and syntrophic mechanisms differentiating methanotrophic and methanogenic archaea. PLoS Biol. 20, e3001508 (2022). [PubMed: 34986141]
45. Malvankar NS, King GM & Lovley DR Centimeter-long electron transport in marine sediments via conductive minerals. ISME J. 9, 527–531 (2014). [PubMed: 25050525]
46. Wegener G, Krukenberg V, Riedel D, Tegetmeyer HE & Boetius A Intercellular wiring enables electron transfer between methanotrophic archaea and bacteria. Nature 526, 587–590 (2015). [PubMed: 26490622]
47. Scheller S, Yu H, Chadwick GL, McGlynn SE & Orphan VJ Artificial electron acceptors decouple archaeal methane oxidation from sulfate reduction. Science 351, 703–707 (2016). [PubMed: 26912857]
48. Shipps C et al. Intrinsic electronic conductivity of individual atomically-resolved amyloid crystals reveals micrometer-long hole hopping via tyrosines. Proc. Natl Acad. Sci. USA 118, e2014139118 (2021). [PubMed: 33372136]
49. Malvankar NS, Mester T, Tuominen MT & Lovley DR Supercapacitors based on *c*-type cytochromes using conductive nanostructured networks of living bacteria. ChemPhysChem 13, 463–468 (2012). [PubMed: 22253215]
50. Neu J et al. Microbial biofilms as living photoconductors due to ultrafast electron transfer in cytochrome OmcS nanowires. Nat. Commun 13, 5150 (2022). [PubMed: 36071037]
51. Alexeyev MF The pKNOCK series of broad-host-range mobilizable suicide vectors for gene knockout and targeted DNA insertion into the chromosome of Gram-negative bacteria. Biotechniques 26, 824–828 (1999). [PubMed: 10337469]
52. Zivanov J et al. New tools for automated high-resolution cryo-EM structure determination in RELION-3. eLife 7, e42166 (2018). [PubMed: 30412051]
53. Zhang K Gctf: real-time CTF determination and correction. J. Struct. Biol 193, 1–12 (2016). [PubMed: 26592709]
54. Pettersen EF et al. UCSF Chimera—a visualization system for exploratory research and analysis. J. Comput. Chem 25, 1605–1612 (2004). [PubMed: 15264254]
55. Glaser F et al. ConSurf: identification of functional regions in proteins by surface-mapping of phylogenetic information. Bioinformatics 19, 163–164 (2003). [PubMed: 12499312]
56. Goddard TD et al. UCSF ChimeraX: meeting modern challenges in visualization and analysis. Protein Sci. 27, 14–25 (2018). [PubMed: 28710774]
57. Case DA et al. The Amber biomolecular simulation programs. J. Comput. Chem 26, 1668–1688 (2005). [PubMed: 16200636]
58. Case DA et al. Amber20 (Univ. California, 2020); https://ambermd.org/CiteAmber.php

Author Manuscript Author Manuscript Author Manuscript Author Manuscript

59. Hornak V et al. Comparison of multiple Amber force fields and development of improved protein backbone parameters. Proteins 65, 712–725 (2006). [PubMed: 16981200]
60. Crespo A et al. Theoretical study of the truncated hemoglobin HbN: exploring the molecular basis of the NO detoxification mechanism. J. Am. Chem. Soc 127, 4433–4444 (2005). [PubMed: 15783226]
61. Henriques J, Costa PJ, Calhorda MJ & Machuqueiro M Charge parametrization of the DvH-c3 heme group: validation using constant-(pH,E) molecular dynamics simulations. J. Phys. Chem. B 117, 70–82 (2013). [PubMed: 23199023]
62. Cruzeiro VWD, Amaral MS & Roitberg AE Redox potential replica exchange molecular dynamics at constant pH in AMBER: implementation and validation. J. Chem. Phys. 149, 072338 (2018). [PubMed: 30134669]
63. Cruzeiro VWD, Feliciano GT & Roitberg AE Exploring coupled redox and pH processes with a force-field-based approach: applications to five different systems. J. Am. Chem. Soc 142, 3823–3835 (2020). [PubMed: 32011132]
64. Jorgensen WL, Chandrasekhar J, Madura JD, Impey RW & Klein ML Comparison of simple potential functions for simulating liquid water. J. Chem. Phys 79, 926–935 (1983).
65. Joung IS & Cheatham TE III Determination of alkali and halide monovalent ion parameters for use in explicitly solvated biomolecular simulations. J. Phys. Chem. B 112, 9020–9041 (2008). [PubMed: 18593145]
66. Darden T, York D & Pedersen L Particle mesh Ewald: An $N\cdot\log(N)$ method for Ewald sums in large systems. J. Chem. Phys 98, 10089–10092 (1993).
67. Ryckaert J-P, Ciccotti G & Berendsen HJ Numerical integration of the cartesian equations of motion of a system with constraints: molecular dynamics of *n*-alkanes. J. Comput. Phys 23, 327–341 (1977).
68. Miyamoto S & Kollman PA Settle: an analytical version of the SHAKE and RATTLE algorithm for rigid water models. J. Comput. Chem 13, 952–962 (1992).
69. Gotz AW et al. Routine microsecond molecular dynamics simulations with AMBER on GPUs. 1. Generalized born. J. Chem. Theory Comput 8, 1542–1555 (2012). [PubMed: 22582031]
70. Beck AD Density-functional thermochemistry. III. The role of exact exchange. J. Chem. Phys 98, 5648–5646 (1993).
71. Stephens PJ, Devlin FJ, Chabalowski CF & Frisch MJ Ab initio calculation of vibrational absorption and circular dichroism spectra using density functional force fields. J. Phys. Chem 98, 11623–11627 (1994).
72. Weigend F & Ahlrichs R Balanced basis sets of split valence, triple zeta valence and quadruple zeta valence quality for H to Rn: design and assessment of accuracy. Phys. Chem. Chem. Phys 7, 3297–3305 (2005). [PubMed: 16240044]
73. Suo B, Shen K, Li Z & Liu W Performance of TD-DFT for excited states of open-shell transition metal compounds. J. Phys. Chem. A 121, 3929–3942 (2017). [PubMed: 28475336]
74. Curutchet C & Mennucci B Toward a molecular scale interpretation of excitation energy transfer in solvated bichromophoric systems. J. Am. Chem. Soc 127, 16733–16744 (2005). [PubMed: 16305264]
75. Russo V, Curutchet C & Mennucci B Towards a molecular scale interpretation of excitation energy transfer in solvated bichromophoric systems. II. The through-bond contribution. J. Phys. Chem. B 111, 853–863 (2007). [PubMed: 17249829]
76. Frisch MJ et al. Gaussian 16 Rev. A.03 (Gaussian, 2016); https://gaussian.com/citation_a03/
77. Jurinovich S, Cupellini L, Guido CA & Mennucci B EXAT: excitonic analysis tool. J. Comput. Chem 39, 279–286 (2018). [PubMed: 29151259]
78. Jurinovich S, Pescitelli G, Di Bari L & Mennucci B A TDDFT/MMPol/PCM model for the simulation of exciton-coupled circular dichroism spectra. Phys. Chem. Chem. Phys 16, 16407–16418 (2014). [PubMed: 24603889]
79. Jurinovich S, Guido CA, Bruhn T, Pescitelli G & Mennucci B The role of magnetic–electric coupling in exciton-coupled ECD spectra: the case of bis-phenanthrenes. Chem. Commun 51, 10498–10501 (2015).

Author Manuscript Author Manuscript Author Manuscript Author Manuscript

80. Graves AB, Graves MT & Liptak MD Measurement of heme ruffling changes in MhuD using UV–vis spectroscopy. J. Phys. Chem. B 120, 3844–3853 (2016). [PubMed: 27035523]
81. Sarkar R, Boggio-Pasqua M, Loos P-F & Jacquemin D Benchmarking TD-DFT and wave function methods for oscillator strengths and excited-state dipole moments. J. Chem. Theory Comput 17, 1117–1132 (2021). [PubMed: 33492950]
82. Adamo C & Jacquemin D The calculations of excited-state properties with time-dependent density functional theory. Chem. Soc. Rev 42, 845–856 (2013). [PubMed: 23117144]
83. Londer YY, Pokkuluri PR, Tiede DM & Schiffer M Production and preliminary characterization of a recombinant triheme cytochrome c7 from *Geobacter sulfurreducens* in *Escherichia coli*. Biochim. Biophys. Acta 1554, 202–211 (2002). [PubMed: 12160993]
84. Skerra A & Schmidt TG Use of the Strep-tag and streptavidin for detection and purification of recombinant proteins. Methods Enzymol. 326, 271–304 (2000). [PubMed: 11036648]
85. Arslan E, Schulz H, Zufferey R, Künzler P & Thöny-Meyer L Overproduction of the *Bradyrhizobium japonicum* c-type cytochrome subunits of the cbb3 oxidase in *Escherichia coli*. Biochem. Biophys. Res. Commun 251, 744–747 (1998). [PubMed: 9790980]
86. Siezen RJ & Leunissen JA Subtilases: the superfamily of subtilisin-like serine proteases. Protein Sci. 6, 501–523 (1997). [PubMed: 9070434]
87. Tang G et al. EMAN2: an extensible image processing suite for electron microscopy. J. Struct. Biol 157, 38–46 (2007). [PubMed: 16859925]
88. Desfosses A, Ciuffa R, Gutsche I & Sachse C SPRING—an image processing package for single-particle based helical reconstruction from electron cryomicrographs. J. Struct. Biol 185, 15–26 (2014). [PubMed: 24269218]
89. Evans R et al. Protein complex prediction with AlphaFold-Multimer. Preprint at bioRxiv 10.1101/2021.10.04.463034 (2022).
90. Zemla A LGA: a method for finding 3D similarities in protein structures. Nucleic Acids Res. 31, 3370–3374 (2003). [PubMed: 12824330]
91. Kumar S et al. MEGA X: molecular evolutionary genetics analysis across computing platforms. Mol. Biol. Evol 35, 1547 (2018). [PubMed: 29722887]
92. Edgar RC MUSCLE: multiple sequence alignment with high accuracy and high throughput. Nucleic Acids Res. 32, 1792–1797 (2004). [PubMed: 15034147]
93. Letunic I & Bork P Interactive Tree Of Life (iTOL) v4: recent updates and new developments. Nucleic Acids Res. 47, W256–W259 (2019). [PubMed: 30931475]

Author Manuscript

Author Manuscript

Author Manuscript

Author Manuscript

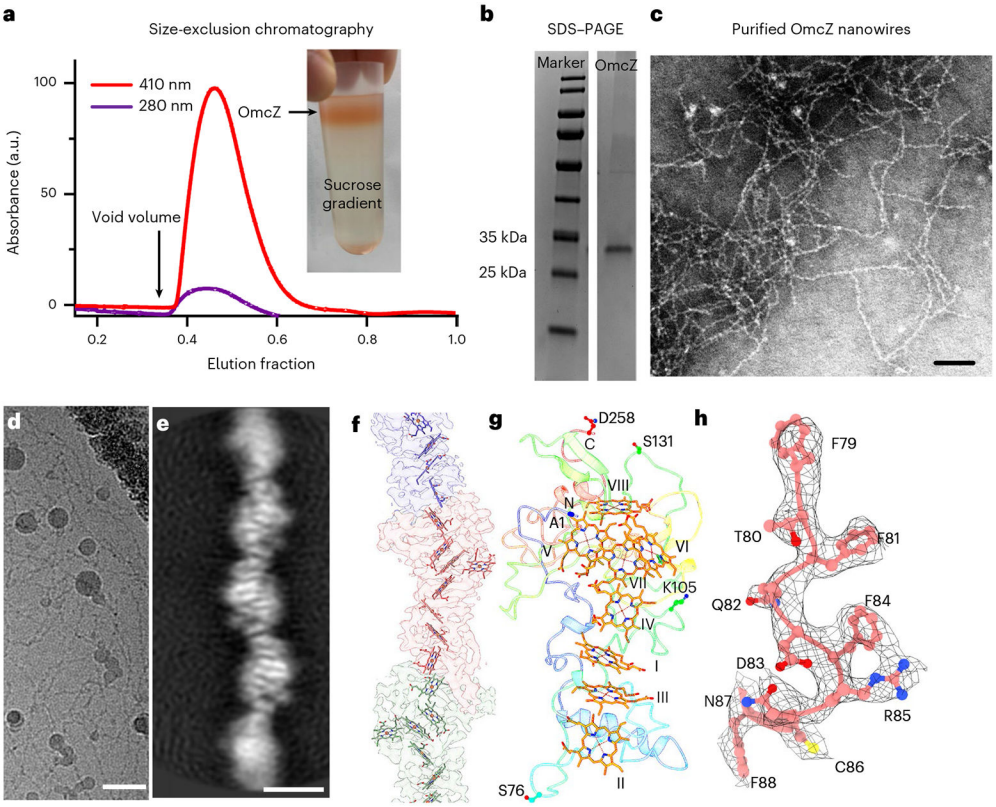

Fig. 1 |. Cryo-EM structure of purified OmcZ nanowires.

a, Size-exclusion chromatography of OmcZ nanowires from *G. sulfurreducens*. The chromatogram of purified sample, showing traces for protein at 280 nm (purple) and haem c at 410 nm (red). Inset: sucrose gradient. **b**, Coomassie-stained SDS–PAGE gel of purified OmcZ nanowires. **c**, Negative-stain TEM image of purified OmcZ nanowires. **d**,**e**, Representative cryo-EM micrograph (**d**) and 2D average (**e**) of purified OmcZ nanowires. Scale bars, 50 nm (**c**), 20 nm (**d**) and 5 nm (**e**). **f**, Highly linear haem chain in OmcZ. **g**, Structure of OmcZ protomer. **h**, Illustration of cryo-EM map quality by fitting sidechains into the EM density.

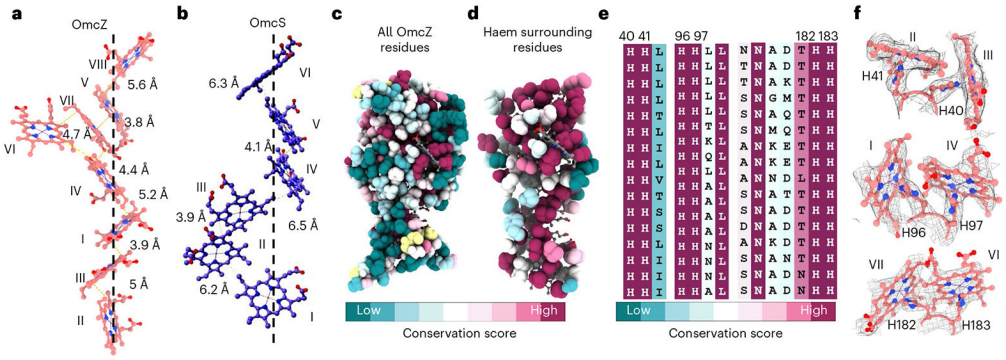

Fig. 2 |. Linear haem arrangement and closer stacking in OmcZ than in OmcS.

a,**b**, Haem arrangement of OmcZ (**a**) versus OmcS protomer (**b**). **c**,**d**, Evolutionary conservation map of all OmcZ residues (**c**) and haem surrounding residues within 4 Å from the haem (**d**). All three consecutive histidine pairs are evolutionarily conserved (**e**) and lock haems more tightly (**f**).

Author Manuscript
Author Manuscript
Author Manuscript
Author Manuscript

Author Manuscript Author Manuscript Author Manuscript Author Manuscript

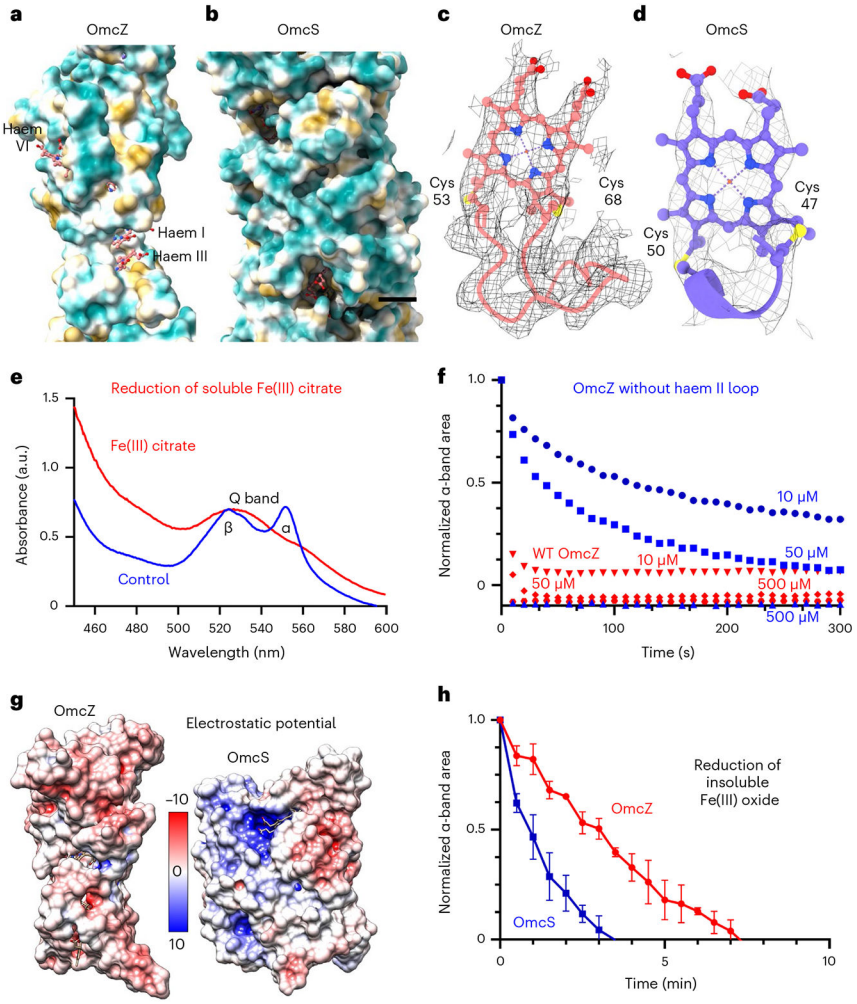

Fig. 3 |. OmcZ nanowires show solvent-exposed haems and non-canonical loop that are involved in electron transfer.

a,**b**, Higher solvent exposure of haems in OmcZ (**a**) and OmcS (**b**) nanowires. **c**,**d**, Haem II binding motif is non-canonical ($CX_{14}CH$) in OmcZ (**c**) versus conventional (CXXCH) in OmcS (**d**). **e**, OmcZ nanowires fully reduce soluble extracellular electron acceptor Fe(III) citrate. **f**, OmcZ without the haem II loop shows a slower reduction rate of Fe(III) citrate than the WT OmcZ nanowires. **g**, Electrostatic potential at pH 7 for OmcZ and OmcS nanowires. **h**, OmcZ nanowires reduce insoluble electron acceptor Fe(III) oxide slower than OmcS nanowires. Values show fraction of reduced cytochrome nanowires as measured by area of α-band absorbance (λ = 543–562 nm) with mean ± standard deviation (n = 3 biological replicates).

Author Manuscript

Author Manuscript

Author Manuscript

Author Manuscript

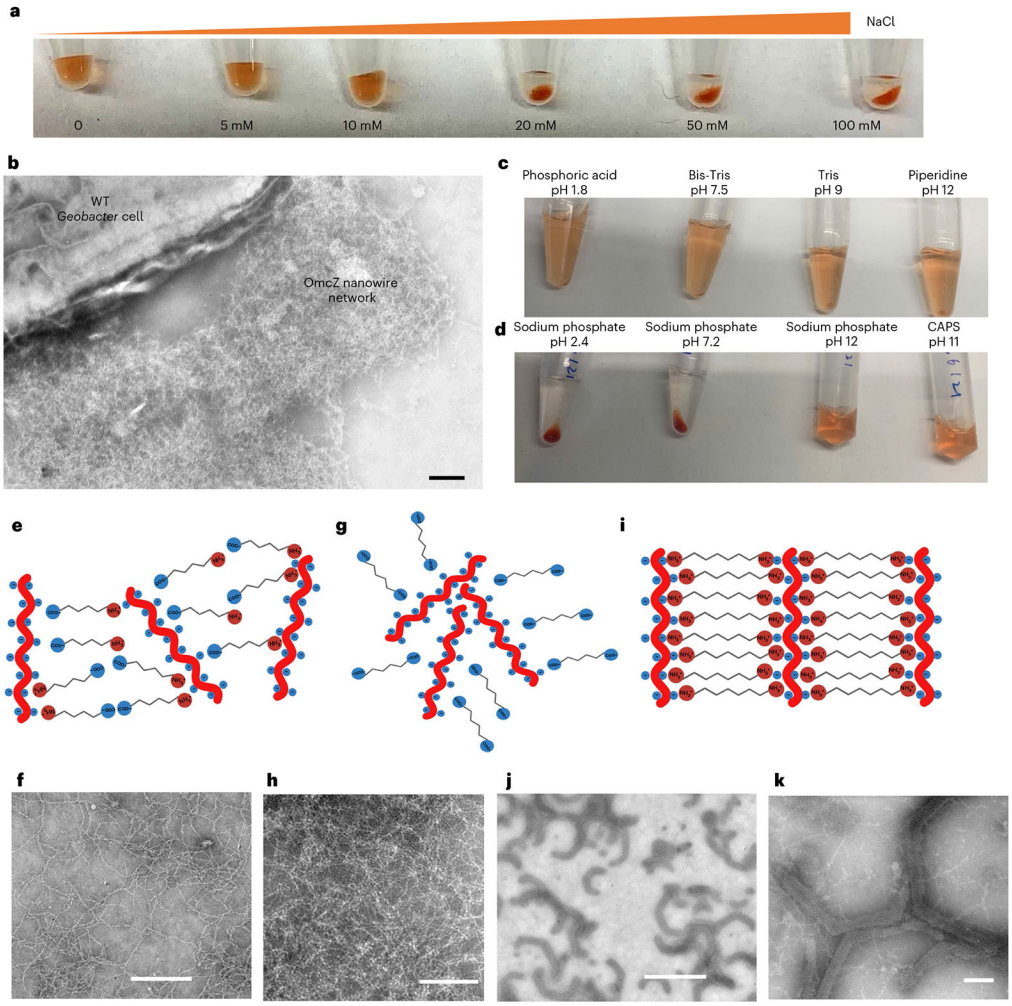

Fig. 4 |. Organization of OmcZ nanowire network changes with biochemical environment. **a**, Solubility of OmcZ nanowires decreases with increasing ionic strength of salt (NaCl). **b**, WT cells form a network of OmcZ nanowires under physiological conditions. **c**, OmcZ nanowires are only soluble in a buffer with low ionic strength **d**, OmcZ nanowires precipitate with increased ionic strength unless the pH is further increased (all buffers are at 20 mM). **e–k**, Schematics and corresponding negative-stain TEM images of supramolecular ordering of OmcZ nanowires: OmcZ nanowires remain aggregated in the presence of 6-aminocapric acid (**e**,**f**); OmcZ nanowires form dense networks with addition of pimelic acid (**g**,**h**); OmcZ nanowires form ordered arrays in the presence of hexamethylenediamine (**i–k**). Scale bars, 20 nm (**k**), 100 nm (**b**,**e**,**f**), 200 nm (**g**,**h**) and 500 nm (**j**).

Author Manuscript Author Manuscript Author Manuscript Author Manuscript

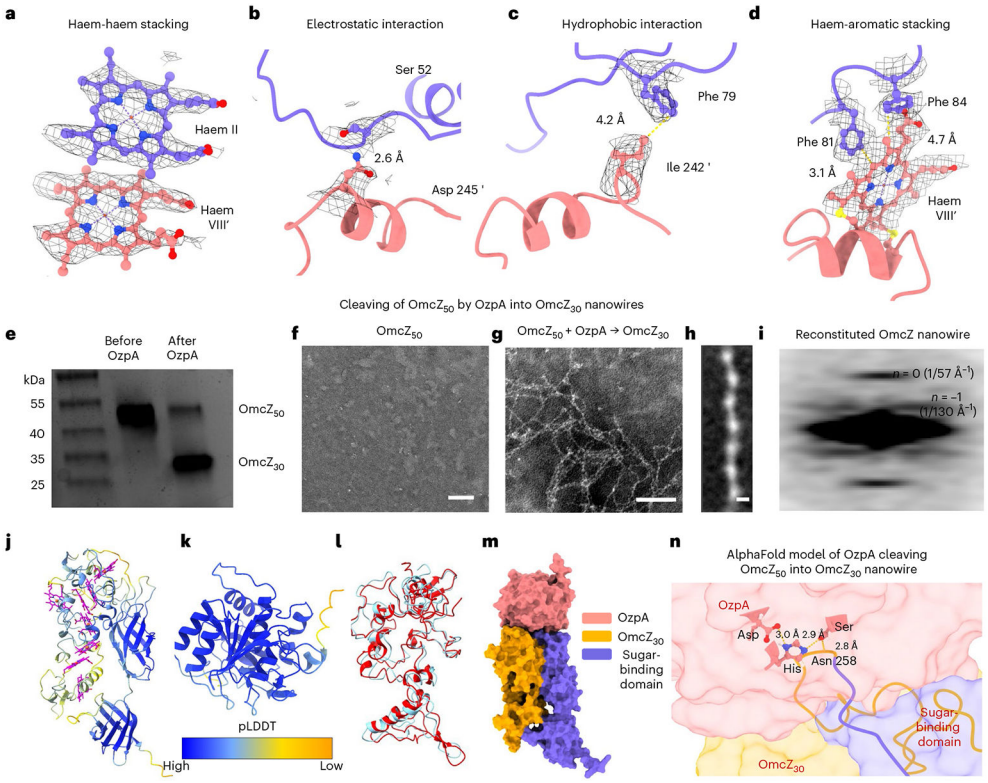

Fig. 5 | A protease-mediated switch regulates OmcZ nanowire assembly.

a–d, Interactions at the OmcZ protomer interface, driving assembly of OmcZ into nanowires, identified in the cryo-EM structure. **a**, Haem-haem stacking interaction. **b**, Electrostatic interaction. **c**, Hydrophobic interaction. **d**, Haemaromatic stacking interaction. **e**, Haem-stained gel showing $OmcZ_{50}$ cleavage by OzpA into nanowire-forming $OmcZ_{30}$. Lane 1: marker. Lane 2: $OmcZ_{50}$ without OzpA. Lane 3: $OmcZ_{50}$ + OzpA (full gel in Supplementary Fig. 1). **f**,**g**, Negative-stain TEM image of $OmcZ_{50}$ into OmcZ nanowires before (**f**) and after (**g**) cleavage by OzpA. **h**,**i**, 2D average (**h**) and averaged power spectrum (**i**) showing reconstituted OmcZ nanowires having nearly identical structure to native nanowires. Scale bars, 100 nm (**f**), 50 nm (**g**) and 2 nm (**h**). **j**,**k**, Side view (**j**) and top view (**k**) of AlphaFold-predicted structure of $OmcZ_{50}$ with confidence (pLDDT) score. **l**, Superimposition of the cryo-EM structure of OmcZ protomer (cyan) and the predicted model of OmcZ (red) showing similar structure. **m**, AlphaFold model of $OmcZ_{50}$ and serine protease OzpA (pink) forming a complex (animations in Supplementary Video 1). $OmcZ_{50}$ contains a cytochrome $OmcZ_{30}$ (yellow) and a sugar binding domain (purple). **n**, Catalytic triad of OzpA is predicted near the cleavage site of sugar-binding domain.

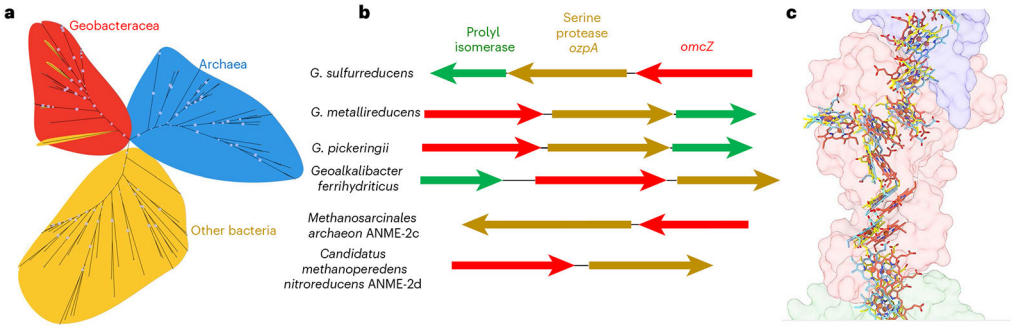

Fig. 6 |. *omcZ* operon homologues are widespread in environmentally important bacteria and archaea.

a, Phylogenetic tree derived from the alignment of amino acid sequences of OmcZ homologues using cut-off score of 100 bit. **b**, The *omcZ* operon homologues are found in diverse bacterial and archaeal species. **c**, Highly similar haem arrangement revealed through superimposed structures of OmcZ nanowire (solved by cryo-EM, red) and *omcZ* homologues (modelled with AlphaFold) from methane oxidizing ANME-2 (cyan) and methanogenic archaea (*Methanosacinales*, yellow) with GenBank IDs MRG77204.1 and CAG1009295.1, respectively.

Author Manuscript
Author Manuscript
Author Manuscript
Author Manuscript